Deng, W., Liu, L., Dai, Y., Wu, H., & Yuan, Z. (2024). A prediction method for blade deformations of large-scale FVAWTs using dynamics theory and machine learning techniques. Energy, 304, Article 132211. Advance online publication. https://doi.org/10.1016/j.energy.2024.132211

A prediction method for blade deformations of large-scale FVAWTs using dynamics theory and machine learning techniques

Wanru Deng[a,c], Liqin Liu[a,*], Yuanjun Dai[b], Haitao Wu[c], Zhiming Yuan[c]

[a] State Key Laboratory of Hydraulic Engineering Intelligent Construction and Operation, Tianjin University, Tianjin, 300072, China

[b] Department of Mechanical and Engineering Science, Peking University, Beijing 100871, China

[c] Naval Architecture, Ocean and Marine Engineering Department, University of Strathclyde, Glasgow, United Kingdom

Abstract

There is renewed interest in floating vertical axis wind turbines (FVAWTs) as offshore wind turbines progressively increase in size and move into deeper waters. To explore the potential of large-scale FVAWTs for future commercialization, it is crucial to investigate blade deformations using an accurate and effective method. In this study, we developed a hybrid model, namely, the SVST-ANN, which integrates dynamic theory and machine learning techniques to predict blade deformations. Specifically, an artificial neural network (ANN) module is incorporated into the slack coupled vertical axis wind turbine simulation tool (SVST), which significantly reduces the total computational time. A comparative study was conducted between the SVST-ANN model and the traditional SVST model, employing a 10 MW helical-type FVAWT as an example. The results show that the SVST-ANN model can accurately and efficiently predict blade deformations. The maximum errors for the maximum value, average value, and standard deviation across all nodes are minimal, with a corresponding computational time reduction of approximately 60%. This study provides a novel method for investigating the dynamic behavior of the FVAWTs, which is more effective for calculating the elastic deformations of blades than traditional numerical methods.

Keywords: Vertical axis wind turbine, Floating wind turbine, Blade deformation prediction, Dynamic response calculation, Machine learning techniques

* Corresponding author at: State Key Laboratory of Hydraulic Engineering Intelligent Construction and Operation, Tianjin University, Tianjin, 300072, China.
E-mail address: liuliqin@tju.edu.cn

Nomenclature for the dynamic modeling process

Coordinate systems:

$\vec{e}^{0}$	Global inertial coordinate system
$\vec{e}^{f}$	Floater body coordinate system
$\vec{e}^{t}$	Tower body coordinate system
$\vec{e}^{b}$	Blade body coordinate system
$\vec{e}_{i}^{k}$	Element coordinate system for the element k of the blade
$\vec{e}^{k}$	Element translation coordinate system for the element k of the blade
$\boldsymbol{A}$	Cardan angles matrix
α , β , γ	Angles rotated in sequence between the coordinate systems

Dynamic modeling for the rigid body:

m	Body mass
$\boldsymbol{J}$	Moment of inertia
$\boldsymbol{\omega}$	Angular velocity
$\boldsymbol{F}$	External forces acting on the rigid body
$\boldsymbol{M}$	Torques acting on the rigid body

Dynamic modeling for the flexible body:

P_0	Arbitrary point on the beam before deformation
P	Arbitrary point on the beam after deformation
$\boldsymbol{r}$	Radius vector of the point P
$\dot{\boldsymbol{r}}$	First derivative of the vector $\boldsymbol{r}$
$\ddot{\boldsymbol{r}}$	Second derivative of the vector $\boldsymbol{r}$
$\boldsymbol{r}_0$	Vector from the origin of the inertial coordinate system to the blade body coordinate system

$\boldsymbol{\rho}_0$	Vector of the point P_0 on the blade floating coordinate system
$\boldsymbol{u}$	Elastic deformation of point P
$\boldsymbol{u}'$	First derivative of the vector $\boldsymbol{u}$ based on the blade body coordinate system
$\boldsymbol{u}''$	Second derivative of the vector $\boldsymbol{u}$ based on the blade body coordinate system
$\boldsymbol{u}^k$	Overall deformation vector of the whole blade
$\boldsymbol{u}_i$	Vector from the element coordinate system to the element translation coordinate system
$\boldsymbol{u}'^k$	Deformation vector on the element translation coordinate system
$u_1'^k$, $u_2'^k$, $u_3'^k$	Elements of the deformation vector on the element translation coordinate system
$\boldsymbol{w}^k$	Non-Cartesian coordinate deformation vector
w_1^k, w_2^k, w_3^k	Elements of the non-Cartesian coordinate deformation vector
N^k	Shape function for the finite element method
N_1^k, N_2^k, N_3^k	Elements of the shape function in tensile and bending directions for the blade node
N_1, N_2, N_3	Elements of the shape function in tensile and bending directions for the whole blade
N_θ	Elements of the shape function in torsional direction for the whole blade
H^k	A shape function matrix represented by N^k
p''^k	Generalized coordinates based on the deformation vector $\boldsymbol{w}^k$
w_{1i}^k, w_{2i}^k, φ_{1i}, w_{3i}^k, φ_{2i}, θ_i	Elements of node i of p''^k, including the tensile deformation, two directions of bending deformation and their corresponding bending angles, and the torsion angle deformation, respectively

w_{1j}^k, w_{2j}^k, φ_{1j}, w_{3j}^k, φ_{2j}, θ_j	Elements of node j of p''^k, including the tensile deformation, two directions of bending deformation and their corresponding bending angles, and the torsion angle deformation, respectively
p'^k	Generalized coordinates based on the deformation vector $\boldsymbol{u}'^k$
u_{1i}^k, u_{2i}^k, φ_{1i}, u_{3i}^k, φ_{2i}, θ_i	Elements of node i of p'^k, including the tensile deformation, two directions of bending deformation and their corresponding bending angles, and the torsion angle deformation, respectively
u_{1j}^k, u_{2j}^k, φ_{1j}, u_{3j}^k, φ_{2j}, θ_j	Elements of node j of p'^k, including the tensile deformation, two directions of bending deformation and their corresponding bending angles, and the torsion angle deformation, respectively
p^k	Generalized coordinates on the blade floating coordinate system
p_0	Overall deformation vector
p	Overall deformation vector after considering the boundary conditions
L^k	Cardan angle matrix between the blade floating coordinate system and the element translation coordinate system
B^k	Boolean matrix
R	Transformation matrix between p and p_0
σ	Normal stress
E	Elastic modulus
ε	Normal strain
τ	Shear stress
G	Shear modulus
γ	Shear strain
K	Stiffness matrix of the elastic beam
K^k	Stiffness matrix of node k
EA, EI_{zz},	Tensile stiffness, two directions of bending stiffness, and

EI_{yy}, GI_p	torsional stiffness of the blade node, respectively
$\hat{\rho}$	Blade density

1. Introduction

Wind energy is a prominent renewable energy source with considerable potential in both onshore and offshore regions [1, 2]. In the last decade, there has been a rapid and substantial increase in the installation of wind turbines as the corresponding technology has gradually matured [3]. The Global Wind Energy Council reported that a total of 77.6 GW of wind power capacity was connected to power grids in 2022, including 68.8 GW from onshore wind turbines and the remainder contributed by offshore wind turbines [4].

Wind turbines can be categorized into horizontal axis wind turbines (HAWTs) and vertical axis wind turbines (VAWTs) according to the orientation of their rotating axes [5]. HAWTs have achieved a long history of successful commercialization in both onshore and offshore markets, driven by advancements in power efficiency and techno-economic feasibility. In contrast, the development of VAWTs has lagged, with the primary developments occurring from the 1970s to 1980s [6]. The initial experiment with a Darrieus-type VAWT took place in 1972, focusing on exploration of the fundamental characteristics [7, 8]. Subsequently, various Darrieus-type turbine concepts were examined and installed in Canada, including Éole, which held the title of the world's largest VAWT with a swept area of 4000 m^2 [9]. Unfortunately, it operated for only five years after installation due to a bottom bearing issue. Concurrently, in the 1970s, a series of VAWT studies were carried out at Sandia National Laboratories (SNL) in the USA. For instance, the well-known Sandia 5-m, 17-m, and 34-m turbines were tested [10-12]. Based on the accumulated technology, more than 500 Darrieus-type VAWTs were successfully operated at the FloWind wind farm in California [13]. Additionally, other VAWT projects, such as VAWT-850 and HM300 [14], were also conducted.

The commercial viability of VAWTs has faced constraints since the 1990s due to several inherent problems, such as significant oscillation of power output and fatigue loading. Nevertheless, renewed interest in VAWT technology for floating offshore applications has emerged, aligning well with two development trends in offshore wind turbines: increased capacity and deeper water depth [15].

The former trend is that larger offshore wind turbines are designed to reduce the levelized cost of electricity. To date, a 15 MW offshore wind turbine with a rotor diameter of 236 m has been launched [16]. By 2030, a power capacity of 20 MW for an offshore wind turbine is expected to be available [17]. However, this trend poses challenges to the operation and maintenance of current FHAWTs. An increasing rotor diameter results in significant vibrations on the blades when subjected to aerodynamic loads and cyclic gravitational load effects. A heavier nacelle raises the center of gravity of the wind turbine system, which has a negative impact on the acceleration sensitivity of the equipment in the nacelle [18]. The installation and maintenance costs are also increased due to the large size of the structure. In contrast, increasing the scale of a FVAWT would not cause such limitations because its generator is mounted at the bottom of the system, resulting in a lower center of gravity and more convenient installation and maintenance. The fatigue problem induced by blade vibrations can be mitigated through the reasonable arrangement of struts. It is expected that the scaling-up limit of the power output of VAWTs can reach 30 MW [19]. The latter trend is the gradual shift of offshore wind turbines into deeper waters to capture vast deep sea wind resources. When the water depth exceeds 60 m, a floating wind turbine is regarded as a more feasible option than a bottom fixed one [20]. For FVAWTs, the fatigue issue at the bottom of the rotor can be alleviated because a floating foundation is employed to reduce the concentrated stress [21].

Consequently, large-scale FVAWTs are of interest because of their great potential for future wind energy applications. Table 1 lists some representative FVAWT concepts proposed in recent years [22-24]. However, it should be noted that research on large-scale FVAWTs is still at its early stage and has not been extensively investigated in the literature.

Table 1 FVAWT concepts

Concept	Capacity	Type of VAWT	Type of floater	Reference
DeepWind	5 MW	Darrieus-type	Spar	[22]
SeaTwirl (S2X)	1 MW	Helical-type	Spar	[23]
VertiWind	2 MW	Helical-type	Semi-submersible	[24]

Aerogenerator X	10 MW	V-shape	Semi-submersible	[25]
SKWID	0.5 MW	H-type	Spar	[26]

To explore the commercial applicability of large-scale FVAWTs, an investigation of their dynamic behavior is essential, and a numerical study on blade deformations is one of the most critical issues. In the early stages, the rigid body dynamic model was applied owing to its simplicity and high efficiency, while the elastic deformations of the tower and blades were ignored. However, the upscaling trend of floating wind turbines facilitates investigation of the significance of blade flexibility. For the blades of a large-scale floating wind turbine, coupling factors originate from inertial loads, composite materials, geometric nonlinearity, and floater motions. These factors have a negative effect on the aerodynamic power output and structural stability and may even lead to severe damage in harsh environments [27].

Many commercial simulation tools, such as Bladed, FAST, and SESAM-Simo, consider the flexibility of blades [28]. However, these tools are restricted to FHAWTs. There is still no publicly available simulation tool specifically designed for the dynamic analysis of FVAWTs, although some research institutions have developed numerical codes for internal use. Borg and Collu [29] programmed a time-domain simulation tool FloVAWT for FVAWTs based on MATLAB/Simulink software. The coupling between environmental loads and the wind turbine structure was considered. The aerodynamic loads were calculated with the application of the double multiple stream tube (DMS) momentum model with some aerodynamic modifications. The hydrodynamic model was implemented based on the Marine Systems Simulator Toolbox. For the mooring system, the force-displacement relation was linearized and the quasi-static catenary method was utilized. Owens et al. [30] developed the OWENS (Offshore Wind Energy Simulation) toolkit for simulating FVAWTs. The tool interfaces with various modules of aerodynamics, hydrodynamics, and multibody dynamics. The floating foundation is assumed to be a rigid body, while the VAWT blade is discretized into beam elements based on the finite element method. Wang et al. [31] developed the coupled numerical code Simo-Riflex-DMS to predict the dynamic behavior of FVAWTs. The time domain simulation is realized based on the coupling of three modules: Simo, Riflex, and DMS. Simo calculates the hydrodynamic forces; DMS calculates the aerodynamic forces; Riflex models the blades, tower, shaft and mooring lines. Cheng et al [32] replaced the

DMS method with the AC method and thus developed the SIMO-RIFLEX-AC simulation tool. Deng et al [33, 34] developed a nonlinear coupled simulation tool for the dynamic modeling and response analysis of FVAWTs. Afterwards, a slack coupled modeling methodology was employed in the simulation tool to improve the calculation efficiency and ensure accurate numerical results [35].

All of the aforementioned numerical codes consider blade flexibility [29-35]. However, when modeling larger-scale FVAWTs, the blade is inevitably divided into more elements. Although this approach enables the capture of dynamic behavior at multiple positions on the blade, it adds the expense of simulation time. Balancing the trade-off between time consumption and the number of blade elements becomes an obstacle, especially when dealing with enormous numerical simulations.

Recently, machine learning approaches have emerged as start-up and highly efficient tools for solving complex nonlinear problems. The core idea is to establish underlying patterns that are useful for understanding relationships in data [36, 37]. Machine learning has a variety of applications in the wind turbine industry, such as power prediction, wind and wave forecasts, and structure optimization. For instance, Wang et al. [38] employed the wavelet transform and a deep convolutional neural network for wind power prediction, demonstrating the robustness of machine learning techniques in capturing nonlinear features of wind power. He et al. [39] proposed a hybrid machine learning approach for short-term wind speed forecasting. The methodology involves employing an ensemble empirical mode decomposition (EEMD) technique for data preprocessing and a kernel-based fuzzy c-means clustering (KFCM) algorithm for data clustering. de N Santos et al. [40] conducted a fatigue estimation of wind turbines based on an artificial neural network (ANN), and measurements for real-world turbines were used as input to realize the estimation. Chen et al. [41] redesigned the equatorial radius, the ratio of the radius over the half-height, and the blade number of a Darrieus-type VAWT by incorporating a heuristic search algorithm into the DMST method. The optimized model exhibited a 12.5% enhancement in the power coefficient at the optimal velocity compared to the baseline.

Motivated by the merits of machine learning techniques, in this study, a hybrid model named SVST-ANN is originally developed for the dynamic modeling and response analysis of large-scale FVAWTs. The system integrates aerodynamics, hydrodynamics, control dynamics, rigid-flexible multibody dynamics, and machine learning algorithms. The coupled numerical code SVST (slack coupled vertical axis wind turbine simulation tool), which was developed in our previous study [35], is first employed to model the wind turbine system and calculate the motions of the floater, deformations of the tower, and deformations on part of the blade elements. Next, the ANN module is incorporated. The blade deformations calculated by the SVST module are selected as input data to predict deformations on other blade nodes. Eventually, the dynamic responses calculated by the two modules are combined; thus, all the dynamic responses of the FVAWT can be derived. This study conducted a series of comparisons between the SVST-ANN model and the traditional SVST model. The results demonstrate that the combination of numerical code and machine learning techniques not only ensures the accuracy of dynamic responses but also significantly reduces the computational time.

The contributions of this study can be summarized as follows:

(1) For the dynamic calculation of FVAWTs, many simulation tools apply the finite element method. When modeling larger-scale FVAWTs, the blade is inevitably divided into more elements, resulting in a significant increase in computational costs. Different from other simulation tools, the hybrid SVST-ANN model developed in this work incorporates an ANN module to predict part of the blade deformations, so that the total computational time can be substantially reduced. To the best knowledge of the authors, no FVAWT simulation tool in the literature combines dynamic methodology with machine learning techniques to predict blade deformations.

(2) For machine learning techniques, many previous studies have attempted to employ neural networks for the short-term prediction of wind turbine dynamic responses. However, it is challenging to directly conduct the long-term prediction due to the cumulative error effect. Compared to previous studies, the SVST-ANN hybrid model uses part of the blade deformations calculated by the SVST module as input data rather than other types of inputs, such as environmental parameters. This approach establishes a stronger mapping between the input and output and effectively avoids cumulative error.

The remaining parts of this paper are organized as follows: A 10 MW helical-type FVAWT is introduced as a test example in Section 2. The traditional SVST model and the proposed SVST-ANN model are presented in Section 3 and Section 4, respectively. In Section 5, a series of comparisons between the two models are conducted and discussed. Finally, the conclusions are summarized in Section 6.

2. Physical problem

This study focuses on a 10 MW helical-type FVAWT system featuring complex helical blades. As illustrated in Fig. 1, the system comprises three blades, a tower, three groups of total nine struts, a floating foundation, and three mooring lines.

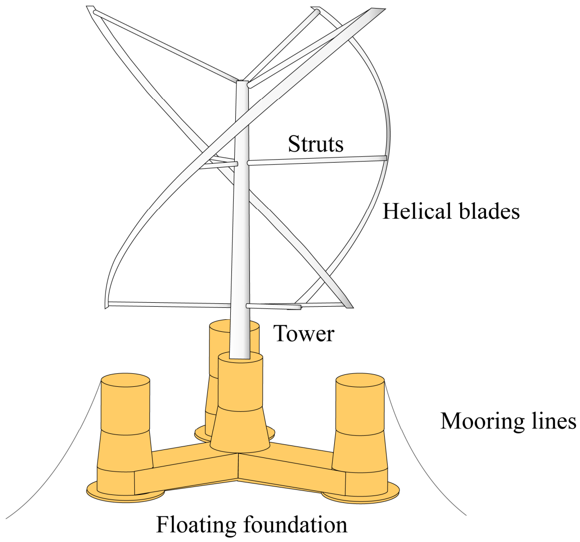

Fig.1 Helical type floating wind turbine system

The concept of a helical-type wind turbine was proposed as an optimization of conventional straight blades or H-type VAWTs to overcome the limitations of large torque fluctuations and poor self-starting performance [42]. The structural definition of the rotor is obtained by upscaling a 5 MW helical-type wind turbine concept [35], given the absence of an existing design in the literature for a benchmark 10 MW FVAWT with helical blades. The classical similarity rules [43] are applied by determining the geometric scaling factor as $\sqrt{2}$ to achieve the doubled power output. Note that the helical twist angle is a vital parameter and is defined as the phase shift angle between the top and bottom of a helical blade. In this study, three blades with a helical twist angle of 120° are applied, as determined in our previous research [44]. For the tower, the diameter increases linearly from the top to the bottom. The position of the top of the tower is designed to match the height of the 3/4 position of the blade, so that the three top struts are slanted to connect the top of the blades and the top of the tower. The detailed parameters of the helical-type wind turbine are listed in Table 2.

Table 2 Parameters of the helical type wind turbine

Item	Value
Rated power	10 MW
Cut-in/Rated/Cut-out wind speed	5/14/25 m/s
Rated rotor speed	0.78 rad/s
Blade number	3
Helical twist angle	120°
Blade length in vertical direction	112 m
Blade chord length	4.1 m
Airfoil	NACA0018
Tower length	143.6 m
Diameter at tower top	5 m
Diameter at tower base	8.3 m
Rotor radius	55 m
Diameter of struts	0.3 m

The floating foundation and mooring system stem from the OO-star semi-submersible concept [45]. The ballast of the floating foundation is slightly adjusted to maintain the draft because the OO-star concept was originally designed for HAWTs. As depicted in Fig. 2, three mooring lines are evenly distributed around the floating foundation with an interval of 120°. A clump mass of 50 t is attached to each mooring line, positioned 118 m from the fairlead. Table 3 provides the specifications of the mooring system. Table 4 presents the main parameters of the helical-type FVAWT system.

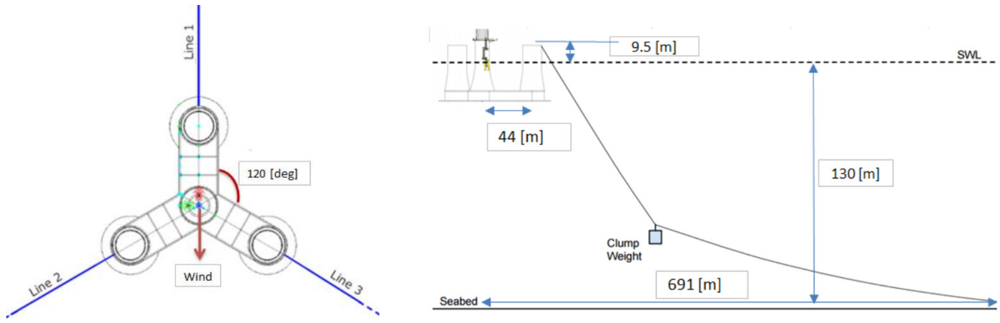

(a) (b)

Fig. 2 Mooring lines arrangement (a) top view (b) side view [45]

Table 3 Parameters of the mooring lines

Item	Value
Number of lines	3
Angle between adjacent lines	120°
Anchor position below MSL	130 m
Vertical position of fairleads above MSL	9.5 m
Mooring line length of upper part (from fairlead to clump mass)	118 m
Mooring line length of lower part (from clump mass to anchor)	585 m
Extensional stiffness	1.506×10^9 N
Equivalent mass per length in air	375.38 kg/m
Equivalent weight per length in water	3200.6 N/m

Table 4 Main parameters of the helical type FVAWT system

Item	Value
Water depth	130 m
Draft	22 m
Total mass (including ballast)	23011.4 t
Center of gravity below MSL (Mean Sea Level)	10.79 m

Elevation of tower base above MSL	11 m

3. SVST model

As introduced above, the helical-type FVAWT is a complex coupling structure comprising numerous components. Therefore, the investigation on its dynamic characteristics necessitates the use of a coupled simulation tool, which spans interdisciplinary research, including aerodynamics, hydrodynamics, control dynamics, and rigid-flexible multibody dynamics. To address this challenge, we propose the numerical code SVST, which integrates the aero-hydro-elastic-control aspects of the FVAWT system. Details of the SVST algorithm can be found in our previous research [35, 44, 46]. Extensive verification works are also included in these publications. For instance, motions of the floater were validated via a code-to-code comparison. The natural frequencies and elastic deformations of the flexible blades were validated against ANSYS software. Satisfactory agreements were obtained in these tests, confirming the accuracy of SVST for dynamic analysis of helical-type FVAWTs.

This section briefly elaborates the theoretical framework and methodology of SVST, starting with an introduction of coordinate systems and their transformation relationships. Then, the dynamic modeling process for flexible blades is presented. Afterwards, the calculation methodologies for environmental loads are explained. Finally, the SVST calculation process is introduced. In addition, for clarity, a nomenclature for the dynamic modeling process is given at the beginning of this paper.

3.1 Definition of coordinate systems

The coordinate systems utilized in SVST are shown in Fig. 3. The global inertial coordinate system ($\vec{e}^{0}$) remains fixed at the center of gravity of the helical type FVAWT system. The floater body coordinate system ($\vec{e}^{f}$) initially coincides with $\vec{e}^{0}$ while moves synchronously with the floater to simulate the six degrees of freedom (DOFs) of motions. The six DOFs include three translational motions of surge, sway, and heave, and three rotational motions of roll, pitch and yaw, which are associated with translational motions, respectively. The surge direction points to the nominal downwind direction. The tower body coordinate system ($\vec{e}^{t}$) is fixed at the tower base for the purpose of calculating the tower elastic deformations, and $\vec{e}^{t}$ is parallel to $\vec{e}^{f}$. The blade body coordinate system ($\vec{e}^{b}$), located at the bottom of the helical blade and rotating with the rotor, is established to depict blade elastic deformations.

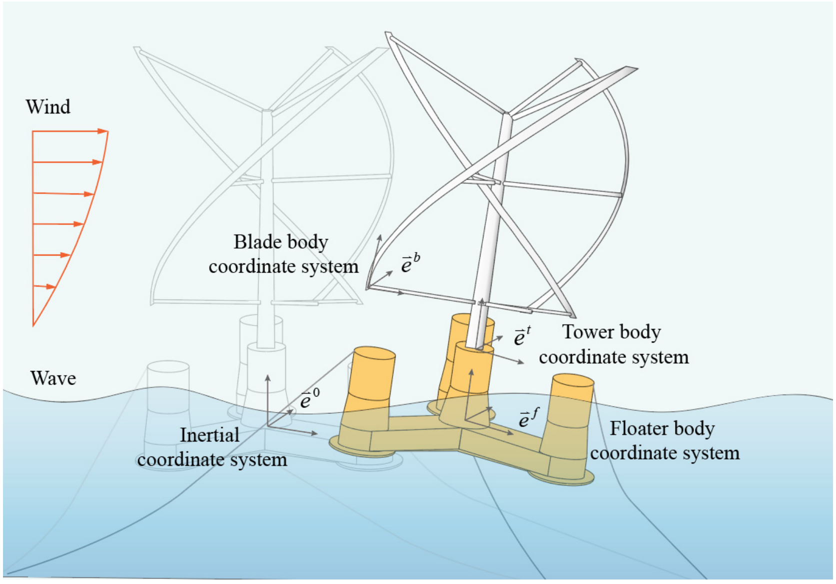

Fig. 3 The FVAWT configuration and the definition of coordinate systems

Various methods, such as Euler angles, Cardan angles and Euler parameters, can be employed to capture the structural posture of the helical-type FVAWT system and describe the transformation relationships between the coordinate systems. In this research, the Cardan angles matrix was applied [47]. As shown in Fig. 4, assuming that a coordinate system undergoes a rotation (from $\boldsymbol{e}^{(0)}$ to $\boldsymbol{e}^{(3)}$), the rotational motion can be decomposed into three steps: (1) the coordinate system $\boldsymbol{e}^{(0)}$ moves to $\boldsymbol{e}^{(1)}$ with rotational angle α; (2) the coordinate system $\boldsymbol{e}^{(1)}$ moves to $\boldsymbol{e}^{(2)}$ with rotational angle β; (3) the coordinate system $\boldsymbol{e}^{(2)}$ moves to $\boldsymbol{e}^{(3)}$ with rotational angle γ. α, β and γ represent the Cardan angles, and the transformation matrix can be written as:

$$\boldsymbol{A}=\begin{bmatrix} \cos\beta\cos\gamma & -\cos\beta\sin\gamma & \sin\beta \\ \cos\alpha\sin\gamma+\sin\alpha\sin\beta\cos\gamma & \cos\alpha\cos\gamma-\sin\alpha\sin\beta\sin\gamma & -\sin\alpha\cos\beta \\ \sin\alpha\sin\gamma-\cos\alpha\sin\beta\cos\gamma & \sin\alpha\cos\gamma+\cos\alpha\sin\beta\sin\gamma & \cos\alpha\cos\beta \end{bmatrix} \quad (1)$$

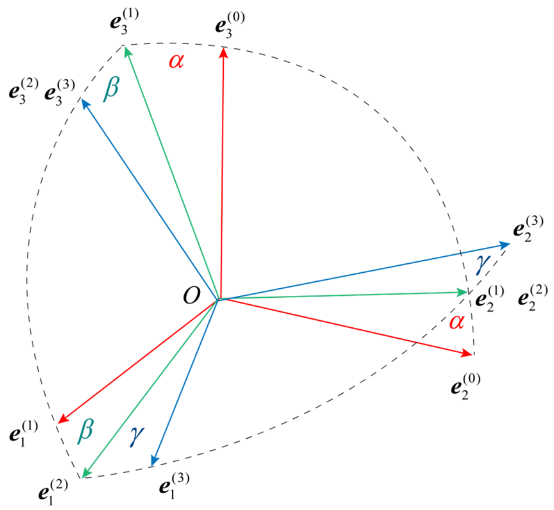

Fig. 4 Cardan angles

3.2 Dynamic modeling for the rigid body

In the dynamic modeling process, the floater and struts are assumed to be rigid bodies, and the momentum theorem of vector mechanics is applied. This theory states that the momentum change of an object is equal to the net external force. Mathematically, it can be expressed as:

$$m\ddot{\boldsymbol{r}} = \boldsymbol{F} \tag{2}$$

$$\boldsymbol{J}\cdot\dot{\boldsymbol{\omega}} + \boldsymbol{\omega}\times\left(\boldsymbol{J}\cdot\boldsymbol{\omega}\right) = \boldsymbol{M} \tag{3}$$

where m is the body mass, $\boldsymbol{J}$ is the moment of inertia, and $\boldsymbol{\omega}$ is the angular velocity. $\boldsymbol{F}$ and $\boldsymbol{M}$ represent the external forces and torques acting on the rigid body.

3.3 Dynamic modeling of a flexible body

The blades and tower are considered as flexible bodies. Here, we use an example of a helical blade to illustrate the modeling method for a flexible body. The prediction of blade deformations is the main focus of this work, so the dynamic modeling process is specifically introduced in this subsection.

Some basic assumptions are first presented: (a) The material of the blade is isotropic, and the constitutive relationship follows Hooke's Law. (b) The material is homogeneous, and the cross-section of the beam is symmetric about its axis. (c) The slender beam model is simplified by neglecting the shear effects.

3.3.1 Kinematic theory

Fig. 5 shows the flexible beam kinematics model. $\vec{e}^0$ is the inertial coordinate system. $\vec{e}^b$ is the blade body coordinate system, which is fixed on the undeformed blade. P_0 represents an arbitrary point on the beam before deformation, and P represents the point after deformation.

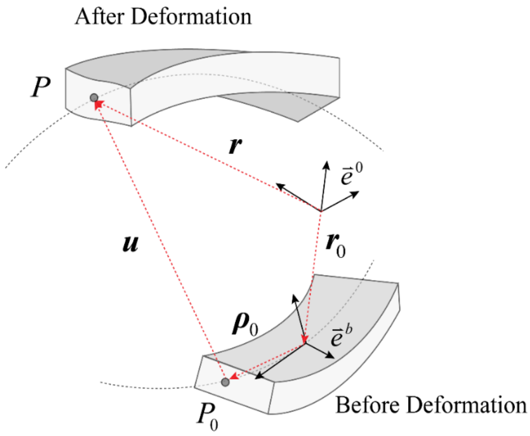

Fig. 5 Flexible beam kinematics

The radius vector $\boldsymbol{r}$ of point P can be written as:

$$\boldsymbol{r} = \boldsymbol{r}_0 + \boldsymbol{\rho}_0 + \boldsymbol{u} \tag{4}$$

where $\boldsymbol{r}_0$ is the vector from the origin of the inertial coordinate system to the blade body coordinate system, representing the large overall motions of the blade. $\boldsymbol{\rho}_0$ is the vector of point P_0 on the blade floating coordinate system. $\boldsymbol{u}$ is the elastic deformation of point P. The first and second derivatives of the vector $\boldsymbol{r}$ can be obtained as follows:

$$\dot{\boldsymbol{r}} = \dot{\boldsymbol{r}}_0 + \boldsymbol{\omega} \times (\boldsymbol{\rho}_0 + \boldsymbol{u}) + \boldsymbol{u}' \tag{5}$$

$$\ddot{\boldsymbol{r}} = \ddot{\boldsymbol{r}}_0 + \dot{\boldsymbol{\omega}} \times (\boldsymbol{\rho}_0 + \boldsymbol{u}) + \boldsymbol{u}'' + \boldsymbol{\omega} \times \boldsymbol{\omega} \times (\boldsymbol{\rho}_0 + \boldsymbol{u}) + 2\boldsymbol{\omega} \times \boldsymbol{u}' \tag{6}$$

where $\boldsymbol{u}'$ and $\boldsymbol{u}''$ are the first and second derivatives of $\boldsymbol{u}$ based on the blade body coordinate system.

3.3.2 Kinetics theory

The helical blade is modeled as a Bernoulli-Euler beam and discretized into numerous straight elements with the application of the finite element method to simulate the elastic deformation $\boldsymbol{u}$. As shown in Fig. 6, a blade is divided into n elements, and each element contains 2 nodes. Each node has 6 DOFs, including tensile deformation, two directions of bending deformation and their corresponding bending angles, and torsion angle deformation. Therefore, a total of 12 DOFs are considered in one element.

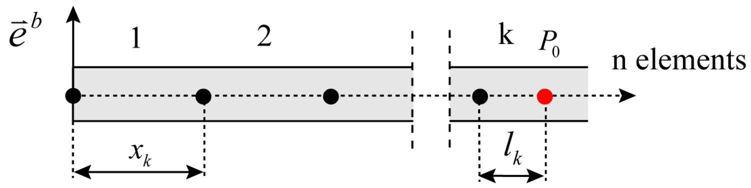

Fig. 6 Finite element method

For the k-th element, the element coordinate system $\vec{e}_i^k$ is defined. Additionally, the element translation coordinate system $\vec{e}^k$ is also employed to facilitate the description of the vector of point P on the element coordinate system, as shown in Fig. 7.

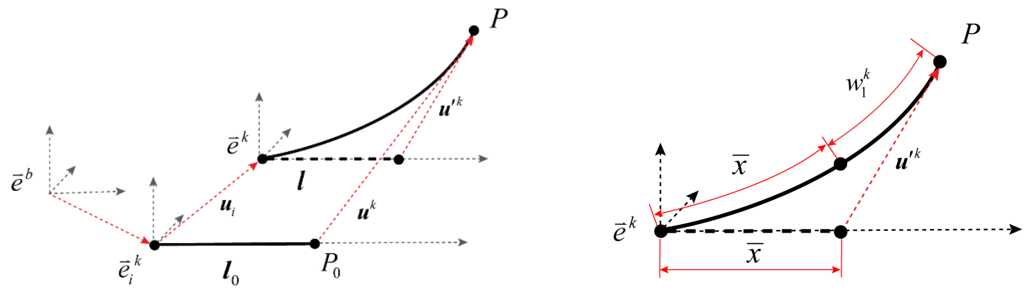

(a) (b)

Fig. 7 Elastic deformation vector of the flexible body (a) element coordinate system (b) element translation coordinate system

Fig. 7(a) presents the deformation vector of point P under the element coordinate system, which can be written as:

$$\boldsymbol{l}_0 + \boldsymbol{u}^k = \boldsymbol{u}_i + \boldsymbol{l} + \boldsymbol{u}'^k \tag{7}$$

where $\boldsymbol{u}_i$ is the vector from the element coordinate system to the element translation coordinate system, $\boldsymbol{u}'^k$ is the deformation vector on the element translation coordinate system. From Eq. (7), $\boldsymbol{u}^k = \boldsymbol{u}_i + \boldsymbol{u}'^k$ can be derived.

As shown in Fig. 7(b), a non-Cartesian coordinate deformation vector $\boldsymbol{w}^k$ can also be defined, where w_1^k represents the axial deformation along the flexible beam. The relationship between the vectors $\boldsymbol{u}'^k$ and $\boldsymbol{w}^k$ can be expressed as follows based on the continuum mechanics theory [48]:

$$\boldsymbol{u}'^{k}=\begin{bmatrix} u_1'^{k} \\ u_2'^{k} \\ u_3'^{k} \end{bmatrix}=\begin{bmatrix} w_1^k-\int_0^{\bar{x}}\frac{1}{2}\left(\frac{\partial w_2^k}{\partial \bar{x}}\right)^2 d\bar{x}-\int_0^{\bar{x}}\frac{1}{2}\left(\frac{\partial w_3^k}{\partial \bar{x}}\right)^2 d\bar{x} \\ w_2^k \\ w_3^k \end{bmatrix} \tag{8}$$

where $\boldsymbol{w}^k$ can be described by using the finite element shape functions:

$$w^k=\begin{bmatrix} w_1^k \\ w_2^k \\ w_3^k \end{bmatrix}=N^k p''^k \tag{9}$$

N^k is the shape function:

$$\begin{aligned} N_1^k &= [N_{11} \quad 0 \quad 0 \quad 0 \quad 0 \quad 0 \quad N_{12} \quad 0 \quad 0 \quad 0 \quad 0 \quad 0] \\ N_2^k &= [0 \quad N_{21} \quad N_{31} \quad 0 \quad 0 \quad 0 \quad 0 \quad N_{22} \quad N_{32} \quad 0 \quad 0 \quad 0] \\ N_3^k &= [0 \quad 0 \quad 0 \quad N_{21} \quad N_{31} \quad 0 \quad 0 \quad 0 \quad 0 \quad N_{22} \quad N_{32} \quad 0] \end{aligned} \tag{10}$$

where:

$$\begin{gathered} N_{11}=1-\frac{x}{l_k} \quad N_{12}=\frac{x}{l_k} \\ N_{21}=1-3\left(\frac{x}{l_k}\right)^2+2\left(\frac{x}{l_k}\right)^3 \quad N_{31}=x-2\frac{x^2}{l_k}+\frac{x^3}{l_k^{\,2}} \\ N_{22}=3\left(\frac{x}{l_k}\right)^2-2\left(\frac{x}{l_k}\right)^3 \end{gathered} \tag{11}$$

p''^k represents the generalized coordinates based on the deformation vector $\boldsymbol{w}^k$, including the 12 DOFs of deformations in one element, which are described in detail in the Nomenclature.

$$p''^k=\begin{bmatrix} w_{1i}^k & w_{2i}^k & \varphi_{1i} & w_{3i}^k & \varphi_{2i} & \theta_i & w_{1j}^k & w_{2j}^k & \varphi_{1j} & w_{3j}^k & \varphi_{2j} & \theta_j \end{bmatrix}^{\mathrm{T}} \tag{12}$$

Similarly, the generalized coordinates p'^k based on the deformation vector $\boldsymbol{u}'^k$ can also be defined as:

$$p'^k=\begin{bmatrix} u_{1i}^k & u_{2i}^k & \varphi_{1i} & u_{3i}^k & \varphi_{2i} & \theta_i & u_{1j}^k & u_{2j}^k & \varphi_{1j} & u_{3j}^k & u_{2j} & \theta_j \end{bmatrix}^{\mathrm{T}} \tag{13}$$

According to Eqs. (7) and (8), the relationship between $\boldsymbol{w}^k$ and $\boldsymbol{u}'^k$ is given by:

$$
\begin{aligned}
u_1'^k &= w_1^k - \frac{1}{2} p'^{k\mathrm{T}} \int_0^{\bar{x}} \left(\frac{\partial N_2^{k\mathrm{T}}}{\partial \bar{x}} \frac{\partial N_2^k}{\partial \bar{x}} + \frac{\partial N_3^{k\mathrm{T}}}{\partial \bar{x}} \frac{\partial N_3^k}{\partial \bar{x}} \right) d\bar{x} p'^k \\
&= N_1^k p'^k + \frac{1}{2} N_{12} p'^{k\mathrm{T}} \int_0^{l_k} \left[\left(\frac{\partial N_2^{k\mathrm{T}}}{\partial \bar{x}} \frac{\partial N_2^k}{\partial \bar{x}} \right) + \left(\frac{\partial N_3^{k\mathrm{T}}}{\partial \bar{x}} \frac{\partial N_3^k}{\partial \bar{x}} \right) \right] d\bar{x} p'^k \\
&\quad - \frac{1}{2} p'^{k\mathrm{T}} \int_0^{\bar{x}} \left(\frac{\partial N_2^{k\mathrm{T}}}{\partial \bar{x}} \frac{\partial N_2^k}{\partial \bar{x}} + \frac{\partial N_3^{k\mathrm{T}}}{\partial \bar{x}} \frac{\partial N_3^k}{\partial \bar{x}} \right) d\bar{x} p'^k
\end{aligned}
\tag{14}
$$

$$
u_2'^k = w_2^k \tag{15}
$$

$$
u_3'^k = w_3^k \tag{16}
$$

where the superscript T represents the matrix transpose. Therefore, the expression of $\boldsymbol{u}'^k$ on the element translation coordinate system is given by:

$$
u'^k = \begin{bmatrix} N_1^k p'^k \\ N_2^k p'^k \\ N_3^k p'^k \end{bmatrix} - \begin{bmatrix} \frac{1}{2} p'^{k\mathrm{T}} H^k p'^k \\ 0 \\ 0 \end{bmatrix} \tag{17}
$$

where H^k is written as:

$$
H^k = -N_{12} \int_0^{l_k} \left(\frac{\partial N_2^{k\mathrm{T}}}{\partial \bar{x}} \frac{\partial N_2^k}{\partial \bar{x}} + \frac{\partial N_3^{k\mathrm{T}}}{\partial \bar{x}} \frac{\partial N_3^k}{\partial \bar{x}} \right) d\bar{x} + \int_0^{\bar{x}} \left(\frac{\partial N_2^{k\mathrm{T}}}{\partial \bar{x}} \frac{\partial N_2^k}{\partial \bar{x}} + \frac{\partial N_3^{k\mathrm{T}}}{\partial \bar{x}} \frac{\partial N_3^k}{\partial \bar{x}} \right) d\bar{x} \tag{18}
$$

3.3.3 Coordinate system transformation

As discussed above, the deformation vector $\boldsymbol{u}'^k$ is derived on the element translation coordinate system. In this subsection, the vector is transformed to the blade floating coordinate system to model the helical blade.

The generalized coordinates of the blade floating coordinate system are supposed as p^k, and the relationship between p^k and p'^k can be given by:

$$
p^k = L^k p'^k \tag{19}
$$

where L^k is the Cardan angle matrix of the element between the blade floating coordinate system and the element translation coordinate system. It should be noted that p^k only includes the information of two nodes on an element, so that the overall deformation vector p_0 is defined, which contains all the deformations along the blade:

$$
p^k = B^k p_0 \tag{20}
$$

where B^k is known as the Boolean matrix [49]. Next, boundary conditions should be introduced for the beam model:

$$p_0 = Rp \tag{21}$$

where p is the overall deformation vector after considering the boundary conditions and R is the transformation matrix.

After the transformation introduced above, the expression $\boldsymbol{u}^k$, which represents the overall deformation vector of the whole blade, can be written as:

$$\boldsymbol{u}^k = A^k \begin{bmatrix} N_1 p \\ N_2 p \\ N_3 p - \frac{1}{2} p^{\mathrm{T}} H p \end{bmatrix} \tag{22}$$

where A^k is the Cardan angle matrix of one node between the blade floating coordinate system and the element translation coordinate system. N_1, N_2 and N_3 are given by:

$$\begin{aligned} N_1 &= N_1^k L^{k\mathrm{T}} B^k R \\ N_2 &= N_2^k L^{k\mathrm{T}} B^k R \\ N_3 &= N_3^k L^{k\mathrm{T}} B^k R \end{aligned} \tag{23}$$

$$H = R^{\mathrm{T}} B^{k\mathrm{T}} L^k H^k L^{k\mathrm{T}} B^k R$$

Note that the above formula derivation only involves the tensile and bending deformations. The derivation process of the torsion angle deformation is similar to that of the tensile deformation. To avoid repetition, the process is not described in this paper; it can be referred to in Ref. [35].

3.3.4 Elasticity theory

According to the assumptions mentioned above, Hooke's Law is utilized, and the shear effects are ignored. Hence, the normal stress is expressed as:

$$\sigma = E\varepsilon \tag{24}$$

where E is the elastic modulus, and ε is the normal strain. The shear stress is written as:

$$\tau = G\gamma \tag{25}$$

where G is the shear modulus, and γ is the shear strain. Then, the stiffness matrix of the elastic beam can be obtained after neglecting the higher-order terms:

$$K = \sum_{k=1}^{n} K^k \tag{26}$$

$$\begin{aligned} K^k = R^{\mathrm{T}} B^{k\mathrm{T}} L^k [& \int_{l_k} EA \left(\frac{\partial N_1}{\partial \bar{x}} \right)^{\mathrm{T}} \left(\frac{\partial N_1}{\partial \bar{x}} \right) d\bar{x} + \int_{l_k} EI_{zz} \left(\frac{\partial^2 N_2}{\partial \bar{x}^2} \right)^{\mathrm{T}} \left(\frac{\partial^2 N_2}{\partial \bar{x}^2} \right) d\bar{x} \\ & + \int_{l_k} EI_{yy} \left(\frac{\partial^2 N_3}{\partial \bar{x}^2} \right)^{\mathrm{T}} \left(\frac{\partial^2 N_3}{\partial \bar{x}^2} \right) d\bar{x} + \int_{l_k} GI_p \left(\frac{\partial^2 N_\theta}{\partial \bar{x}^2} \right)^{\mathrm{T}} \left(\frac{\partial^2 N_\theta}{\partial \bar{x}^2} \right) d\bar{x}] L^{k\mathrm{T}} B^k R \end{aligned} \tag{27}$$

where EA, EI_{zz}, EI_{yy}, and GI_p are the tensile stiffness, two directions of bending stiffness, and torsional stiffness of the blade node, respectively.

3.3.5 Jourdain's velocity variational principle

The dynamic equilibrium of the flexible blade system can be expressed as the following equation based on Jourdain's velocity variational principle.

$$\int_V \delta \dot{r}^{\mathrm{T}} \hat{\rho} \ddot{r} dV + \delta \dot{p}^{\mathrm{T}} Kp - \delta W_b = 0 \tag{28}$$

in which $\int_V \delta \dot{r}^{\mathrm{T}} \hat{\rho} \ddot{r} dV$ represents the variation of kinetic energy, and $\hat{\rho}$ is the blade density. $\delta \dot{p}^{\mathrm{T}} Kp$ represents the variation of kinetic energy. δW_b represents the variation of external force energy. The methodologies for simulating external forces are discussed in subsection 3.4.

3.4 Environmental loads

The dynamic responses of a helical type FVAWT are governed by the combined actions of its inertia as well as offshore environmental loads, such as aerodynamic loads on the blades and tower, and hydrodynamic loads on the floater and mooring lines. Additionally, the coupling effect between environmental loads and the structure needs to be properly considered to evaluate the structural ability to withstand fatigue. The detailed methodologies for determining environmental loads have been extensively described in our previous research [35, 46]. To avoid redundancy, we provide a concise overview of the algorithms in this subsection.

For aerodynamic loads, the unsteady blade element momentum (UBEM) method with aerodynamic corrections is utilized [50]. The UBEM was inspired by the conventional blade element momentum (BEM) method for HAWTs, which was initially proposed by Rankine [51] and Froude [52]. The UBEM is conducted in the time domain, considering time-delay effects caused by dynamic wakes or dynamic inflows. Fig. 8 shows the blade velocity vector. The blade azimuth angle θ varies as the wind turbine rotates. The relative inflow velocity V_{rel} can be derived considering the incoming wind speed, rotational speed, and the motions of the floating foundation. Based on momentum theory, the induction factor of the blade can be obtained through momentum loss and rotor thrust, and induction factors converge throughout the time domain process. During this process, the normal force and tangential force can be calculated based on the transformation relationships among the relative inflow velocity V_{rel}, normal inflow velocity $V_{rel,n}$, and tangential inflow velocity $V_{rel,t}$. Subsequently, the aerodynamic parameters of the rotor can be obtained, such as the thrust, torque, and power.

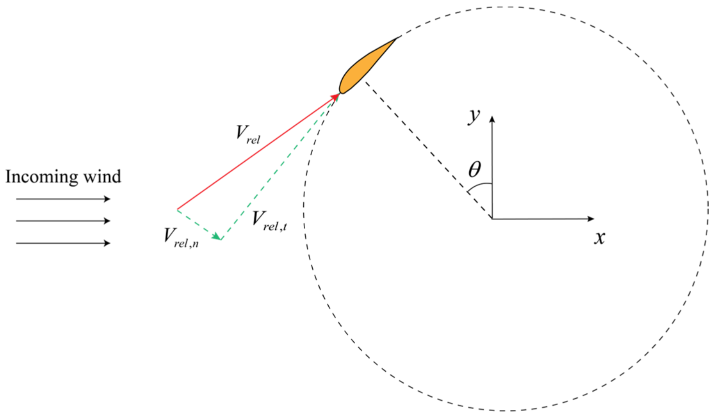

Fig. 8 Blade velocity vector

Additionally, aerodynamic corrections are included to improve the accuracy of the UBEM. Dynamic stall is considered based on the B-L model proposed by Beddoes and Leishman [53]. This model simulates three stages: full attached flow, trailing-edge flow separation, and dynamic stall (complete separation flow) [54, 55]. Prandtl's tip-loss theory is employed to adjust the lift and drag coefficients [56]. Additionally, a dynamic inflow correction is utilized to balance the relationship between the thrust and induction velocity caused by the aerodynamic load variation [57].

Hydrodynamic loads are derived based on the DNVGL software SESAM [58]. Linear wave theory and the 3D potential flow method are utilized based on the assumptions that the water flow is inviscid and irrotational and that the wave amplitude is much smaller than the wavelength. Fig. 9 shows the hydrodynamic model established in SESAM. The hydrodynamic coefficients and wave force transfer functions in the frequency domain are calculated by the analysis program WADAM, including linear and quadric transfer functions, radiation coefficients, and hydrodynamic restoring force coefficients. The frequency domain parameters are then introduced to the hydrodynamic module of the SVST so that they can be transferred into time domain hydrodynamic loads.

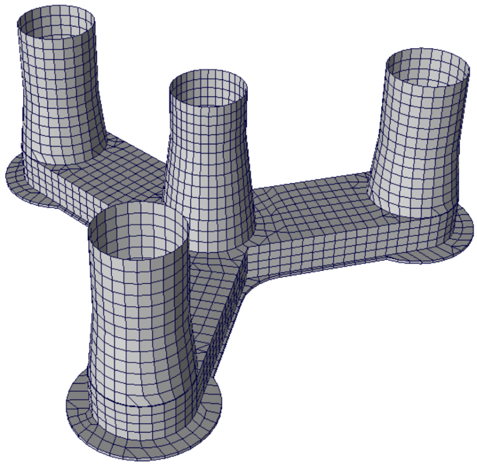

Fig. 9 Hydrodynamic model in SESAM

The mooring forces are computed using the quasi-static catenary method [59]. This method assumes that the mooring lines maintain static equilibrium at any time. The mooring line is divided into several elements. For each element, the force equilibrium equation can be obtained by neglecting the inertia and hydrodynamic effects. After integrating the element forces along the catenary line from the anchor to the fairlead, the instantaneous tension of the mooring lines can be simulated.

3.5 SVST model calculation process

Based on dynamic theories, the coupled numerical code SVST was developed to simulate the time-domain dynamic behavior of a helical-type FVAWT. As introduced above, the helical type FVAWT is a complex multi-body system. To simulate its dynamic responses, numerous coordinate systems are defined, leading to a large and intricate dynamic equation. Hence, the SVST code employs a slack coupled methodology to streamline equation solving and improve solution efficiency [35].

Fig. 10 shows a schematic diagram of the slack coupled modeling method. The wind turbine system is divided into two configurations. Configuration 1 consists of a rigid-flexible coupling system, where the floater and blades are modelled as rigid bodies, while the tower is treated as a flexible beam. Configuration 2 models the blades as flexible beams. During the time domain simulation, the motions of rigid blades are computed in configuration 1 at each timestep and then transferred to configuration 2 as the overall motions of the flexible blades. Compared to the fully coupled method, the slack coupled method simplifies the coupling relationship between the blades and substructures by disregarding the effect of blade deformation on substructures. Using this method, the SVST code ensures accurate results while reducing the time consumption of numerical calculations for helical type FVAWTs.

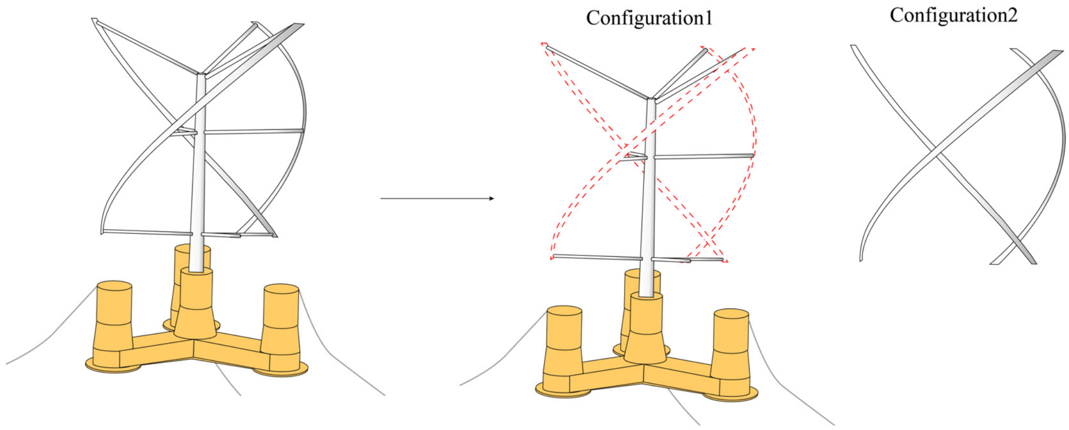

Fig. 10 Schematic diagram of the slack coupled modeling method

Fig. 11 illustrates the computational flowchart for the SVST numerical code. Prior to the time domain simulations, the initial parameters, including the hydrodynamic parameters, environmental conditions, and structural positions, are pre-set within the code. Then, the environmental loads and constraint equations are incorporated into configuration 1 to form the Lagrange equation. This equation calculates the dynamic responses in configuration 1, including the floater motions, tower deformations, and large overall blade motions. Afterwards, configuration 1 provides the time histories of large overall blade motions to configuration 2 as boundary conditions. Finally, configuration 2 computes the blade elastic deformations.

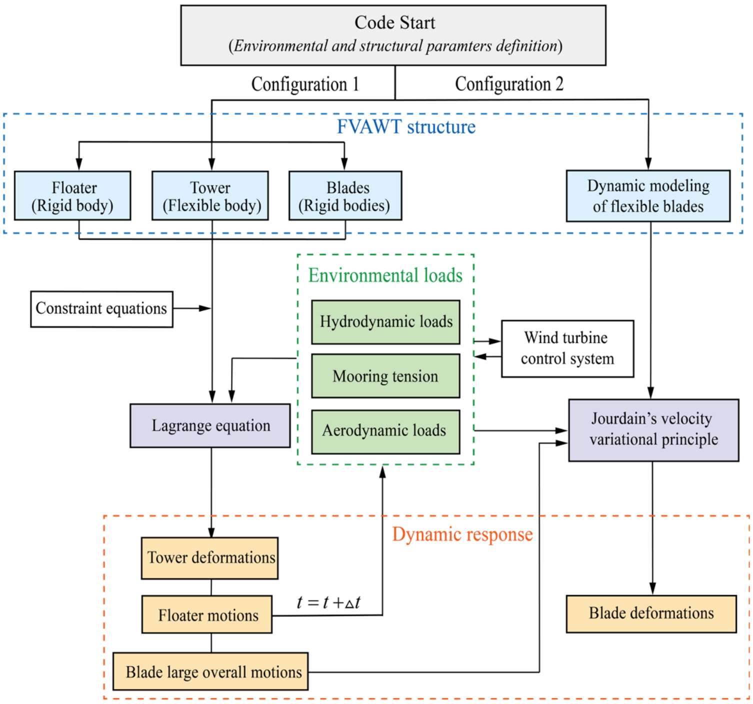

Fig. 11 Computational flowchart for the SVST

4. SVST-ANN hybrid model

This section introduces the hybrid SVST-ANN model proposed in this study, which combines machine learning techniques with the SVST numerical code to enhance computational efficiency. The core idea is to compute the blade deformations on some specific nodes using the SVST module and predict the deformations on other nodes using the ANN module.

4.1 ANN structure

Although numerous complex neural network architectures have been proposed, this study employs the typical ANN owing to its robust ability to simulate nonlinear mappings [60]. As illustrated in Fig. 12, the ANN follows a common structure comprising an input layer, one or several hidden layers, and an output layer. The neurons within each layer are linked to each other in various layers of the network. The input layer receives blade deformations on some key nodes, which are derived from the SVST module. The hidden layer, situated between the input and output layers, carries out computations to find features and patterns of blade deformations on different nodes.

Finally, the output layer is responsible for predicting the blade deformations on other nodes that are not calculated by the SVST module.

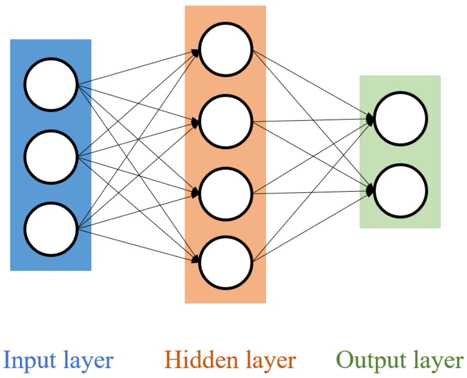

Fig. 12 The ANN models

4.2 Calculation process of the SVST-ANN model

Based on the integration of the ANN algorithm, the SVST-ANN hybrid model is established using MATLAB software to calculate the dynamic responses of helical-type FVAWTs. Fig. 13 shows the flowchart of the system which can be divided into three steps:

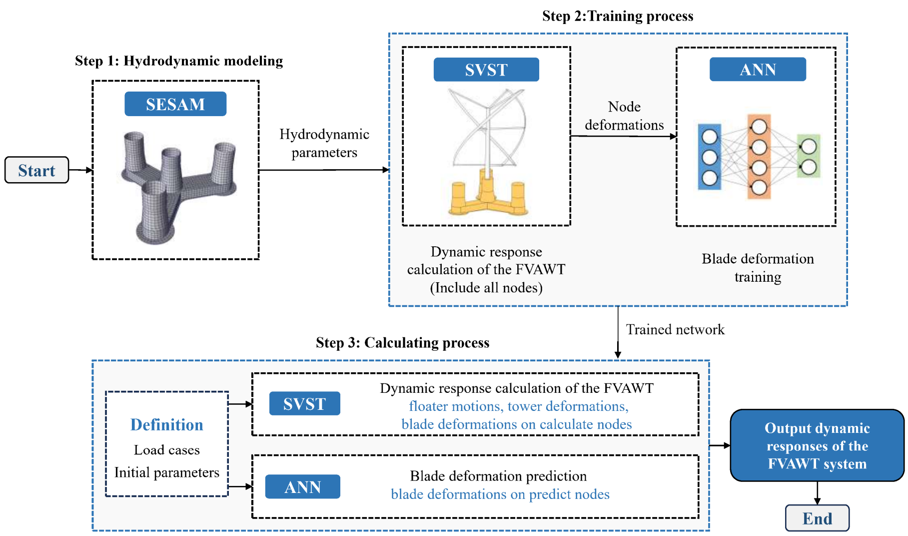

Fig. 13 The flowchart of SVST-ANN system

Step 1: Hydrodynamic modeling

In the first step, a hydrodynamic model is established in SESAM with the input parameters of the helical type FVAWT system. The hydrodynamic coefficients and wave force transfer functions in the frequency domain are then computed using the analysis program WADAM.

Step 2: Training process

The helical type FVAWT is modeled utilizing the SVST numerical code with the incorporation of hydrodynamic parameters. Next, the SVST computes helical blade deformations under various environmental conditions to generate training data. During this process, the finite element method discretizes the helical blades into numerous elements. The deformations of specific key nodes, named calculate nodes, are manually selected as the input data, while the deformations of other nodes, named predict nodes, are considered as the output data.

Afterwards, the training data are input into the ANN module, and the hyperparameters are tuned, such as the number of hidden layers, the number of neurons, and the learning rate. The training process continues until the loss function, defined as the mean square error (MSE), reaches a sufficiently low value. Consequently, the network for the prediction of blade deformations is modeled. The trained network is exported to establish the SVST-ANN calculation system.

Step 3: Calculation process

The established hybrid SVST-ANN model is applied to compute the dynamic responses of the helical type FVAWT. For a specific load case, environmental parameters are first defined. The SVST and ANN modules conduct time series simulations simultaneously. It is noteworthy that fewer blade elements are divided in the SVST module during the blade modeling process, only focusing on the calculate nodes. At each timestep, the SVST module calculates the floater motions, tower deformations, and blade deformations on the calculate nodes. Afterwards, blade deformations on these calculate nodes are introduced into the ANN module as input to predict the blade deformations on the predict nodes.

5 Results and discussion

In this section, a comparison of blade deformations between the SVST and SVST-ANN models is described to demonstrate the accuracy and efficiency of the proposed

SVST-ANN hybrid model in predicting the dynamic responses of a helical type FVAWT. The parameters of the two models are first introduced. Then a comprehensive comparison is conducted, involving temporal histories, spatial trajectories, and statistical results. Finally, the computational costs of the two models are compared.

5.1 Parameter setting

The 10 MW helical-type FVAWT introduced in Section 2 was modeled using the SVST-ANN and SVST methods. Fig. 14 shows the top view of a helical blade. In the SVST model, each helical blade is discretized into 20 elements with 21 nodes. For comparison, during the training process of the SVST-ANN model, the blade is also divided into 20 elements. As shown in Fig. 15, three boundary nodes (marked in red) are located at the top, middle, and bottom of the blade, exhibiting zero deformation owing to the restriction of struts. The remaining 18 nodes are divided into two groups: 8 nodes (marked in blue) represent the calculate nodes, and 12 nodes (marked in yellow) represent the predict nodes. Therefore, during the calculation process of the SVST-ANN model, the blade is divided into 10 elements in the SVST module, which contain only the calculate nodes. The blade deformation on a node is divided into the *x*- and *y*-directions based on the blade coordinate system. The deformations in the two directions are trained respectively using the ANN module.

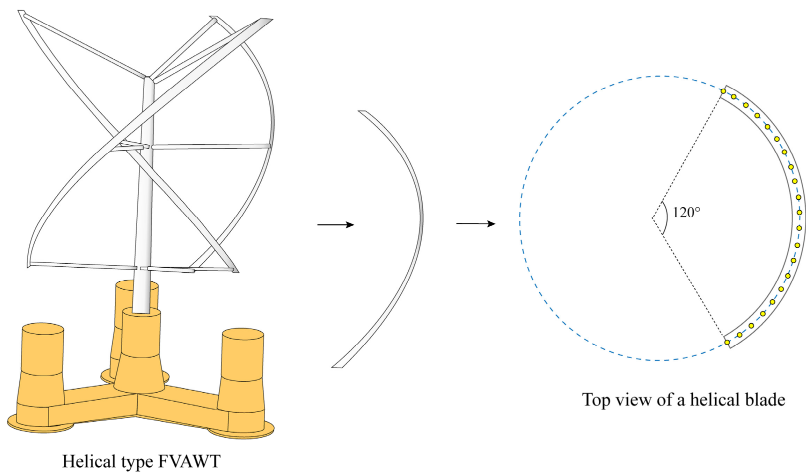

Fig. 14 Top view of a helical blade

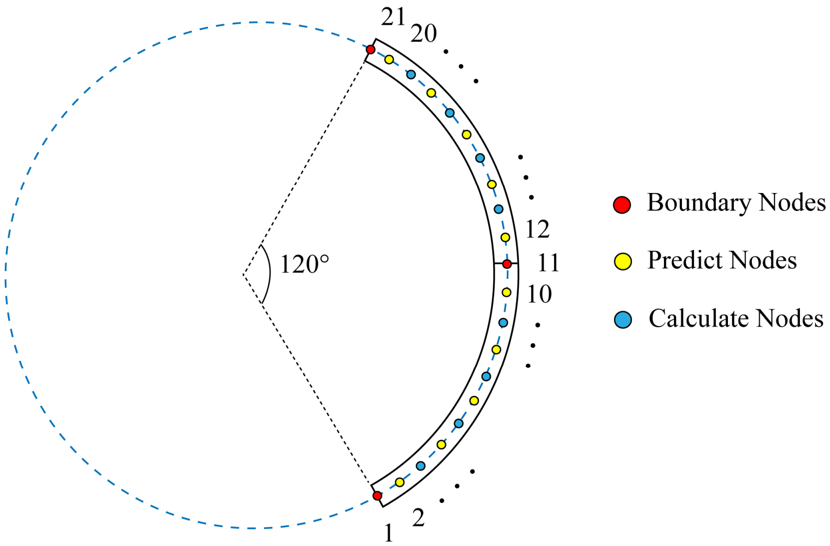

Fig. 15 Distribution of nodes on the blade

The hyperparameters of the ANN are carefully tuned because they are significantly related to the prediction performance. Ultimately, two hidden layers, each containing 20 neurons, were employed, and the Levenberg-Marquardt backpropagation algorithm was utilized. The mean wind speeds ranging from a cut-in wind speed of 5 m/s to a cut-out wind speed of 25 m/s, with 2 m/s steps, were used as training cases. The wave parameters were selected according to the measured data from the Gulf of Maine [61]. Environmental parameters of the training cases are shown in Table 5. For these cases, irregular waves and turbulent wind were considered. The wind and waves coincide, aligning with the surge motion, as shown in Fig. 3. For each case, a time series of 400 s of blade deformations was used as training data after removing a small part of initial start-up transients. The trained network was exported to conduct the calculating process of the SVST-ANN hybrid model.

Table 5 Environmental parameters of the training cases

Load cases	Mean wind speed	Wind turbulence intensity	Significant wave height	Spectral peak period
LC 1.1	5 m/s	4.1%	1.38 m	7.00 s
LC 1.2	7 m/s	4.7%	1.66 m	7.95 s
LC 1.3	9 m/s	5.1%	1.98 m	8.00 s

LC 1.4	11 m/s	5.4%	2.36 m	8.29 s
LC 1.5	13 m/s	5.7%	2.83 m	9.13 s
LC 1.6	15 m/s	6.0%	3.38 m	9.64 s
LC 1.7	17 m/s	6.2%	4.01 m	9.89 s
LC 1.8	19 m/s	6.3%	4.79 m	10.65 s
LC 1.9	21 m/s	6.4%	5.70 m	11.85 s
LC 1.10	23 m/s	6.5%	6.85 m	12.00 s
LC 1.11	25 m/s	6.7%	8.31 m	12.34 s

To compare the SVST and SVST-ANN models, several testing cases were defined. The environmental parameters are shown in Table 6. LC 2.1, which is an untrained load case, was selected to test the prediction capability of the SVST-ANN model under untrained scenarios. In addition, it is essential to explore whether the SVST-ANN model can effectively forecast blade deformations when the environmental parameters change. Therefore, LC 2.2, LC 2.3 and LC 2.4 were defined. Compared to LC2.1, LC 2.2 has a different mean wind speed and rotational speed, LC 2.3 has different inflow turbulence, and LC 2.4 has different significant wave height and spectral peak period. When generating wind and waves, the random seed was changed for each case.

Table 6 Environmental parameters of the testing cases

Load cases	Mean wind speed	Wind turbulence intensity	Rotational speed	Significant wave height	Spectral peak period
LC 2.1	14 m/s	6 %	0.78 rad/s	3.10 m	9.39 s
LC 2.2	20 m/s	6 %	0.65 rad/s	3.10 m	9.39 s
LC 2.3	14 m/s	12 %	0.78 rad/s	3.10 m	9.39 s
LC 2.4	14 m/s	6 %	0.78 rad/s	6 m	11 s

The time-domain simulations for the two models were conducted separately on a Core (TM) i7-13700F CPU@2.1GHz server with a 5.2GHz 30GB RAM, simulating for 2000 s with a time interval of 0.1 s. Noticeably, the SVST-ANN model also calculates other dynamic responses of the helical type FVAWT, including floater motions and tower deformations. Nevertheless, both the SVST and SVST-ANN models employ the configuration 1 of SVST module to compute these dynamic responses, resulting in no difference between them. Therefore, only the blade deformations are compared and discussed.

The remaining parts of this section are organized as follows: subsection 5.2-5.5 specifically compare the SVST model and SVST-ANN model under LC 2.1, including temporal features, spatial features and statistical results of blade deformations, as well as the computational time of the two models. Subsection 5.6 demonstrates the prediction ability of SVST-ANN model under LC 2.2-2.4.

5.2 Temporal features

Fig. 16 shows the temporal comparison of blade deformations in the x and y directions. The horizontal axis represents time, and the vertical axis represents blade deformation components. A duration from 500 s to 550 s was chosen to clearly present the variation of deformations. The schematic diagram on the right side displays the corresponding numbers and positions of the blade nodes. In addition, only the deformations on the lower half of the blade are presented in the figure since the deformation patterns are identical for the upper and lower halves [44].

The two curves derived by the SVST and SVST-ANN models match well, indicating the precise predictive capability of the SVST-ANN model for the nonlinear behavior of blade deformations. For the calculate nodes (marked in yellow), a minimal difference is observed in the figure, which is attributed to the element variation in the finite element method. Although both models use the same SVST module to calculate blade deformations on these nodes, the SVST model divides the helical blade into 20 elements, while the SVST-ANN model divides it into 10 elements. For the predict nodes (marked in blue), the temporal results of the two models exhibit good agreement. For node 2, there is a slight distinction observed in the x-direction. This discrepancy may partly stem from the inherent structural characteristics of the blade. The tangential stiffness of the blade airfoil is substantially larger than the normal stiffness, contributing to a much smaller blade deformation of node 2 in the *x*-direction compared to the *y*-direction. Despite the normalization method was employed during the training process, a small bias inevitably occurred when predicting the blade deformation in the *x*-direction of node 2.

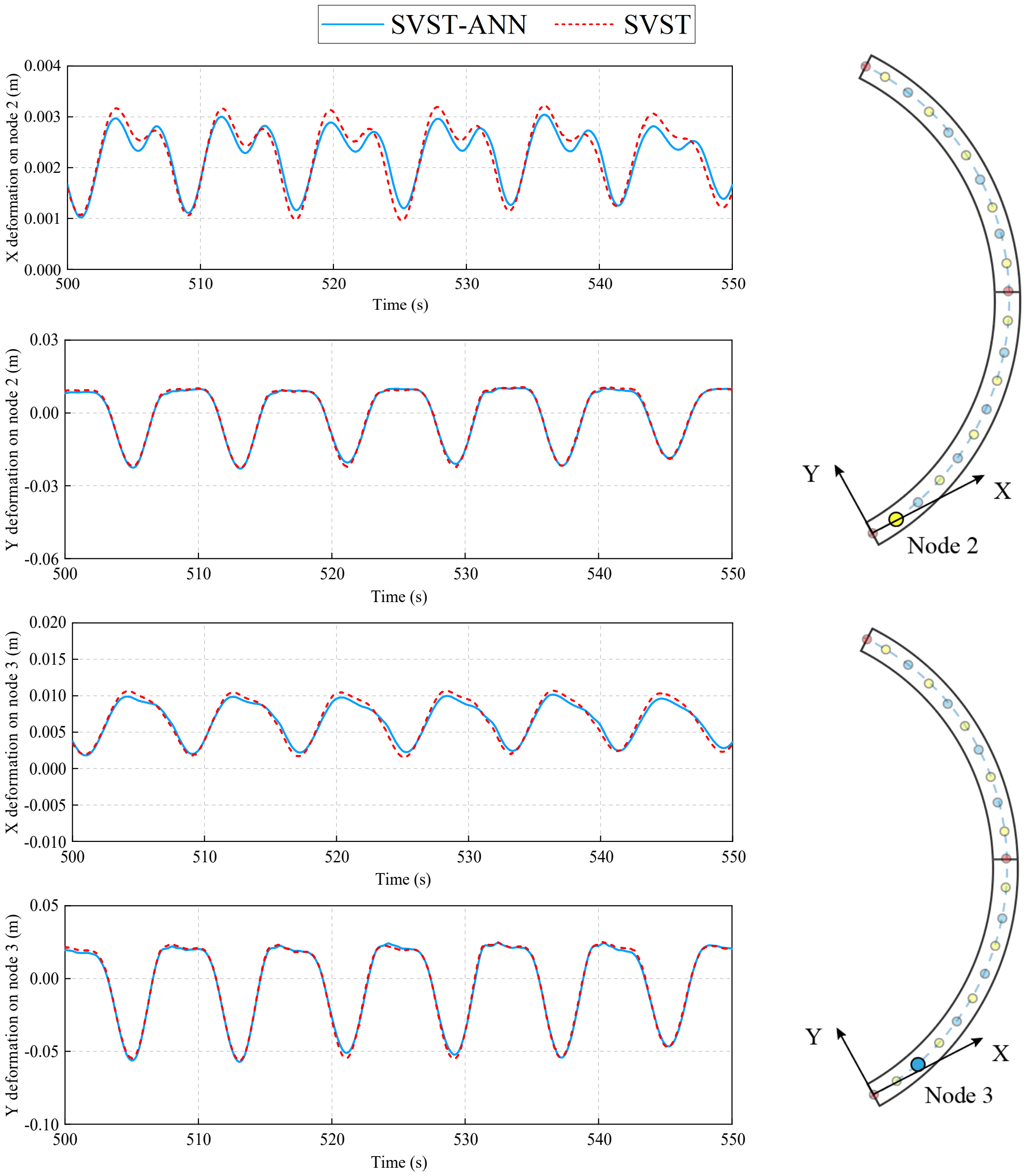

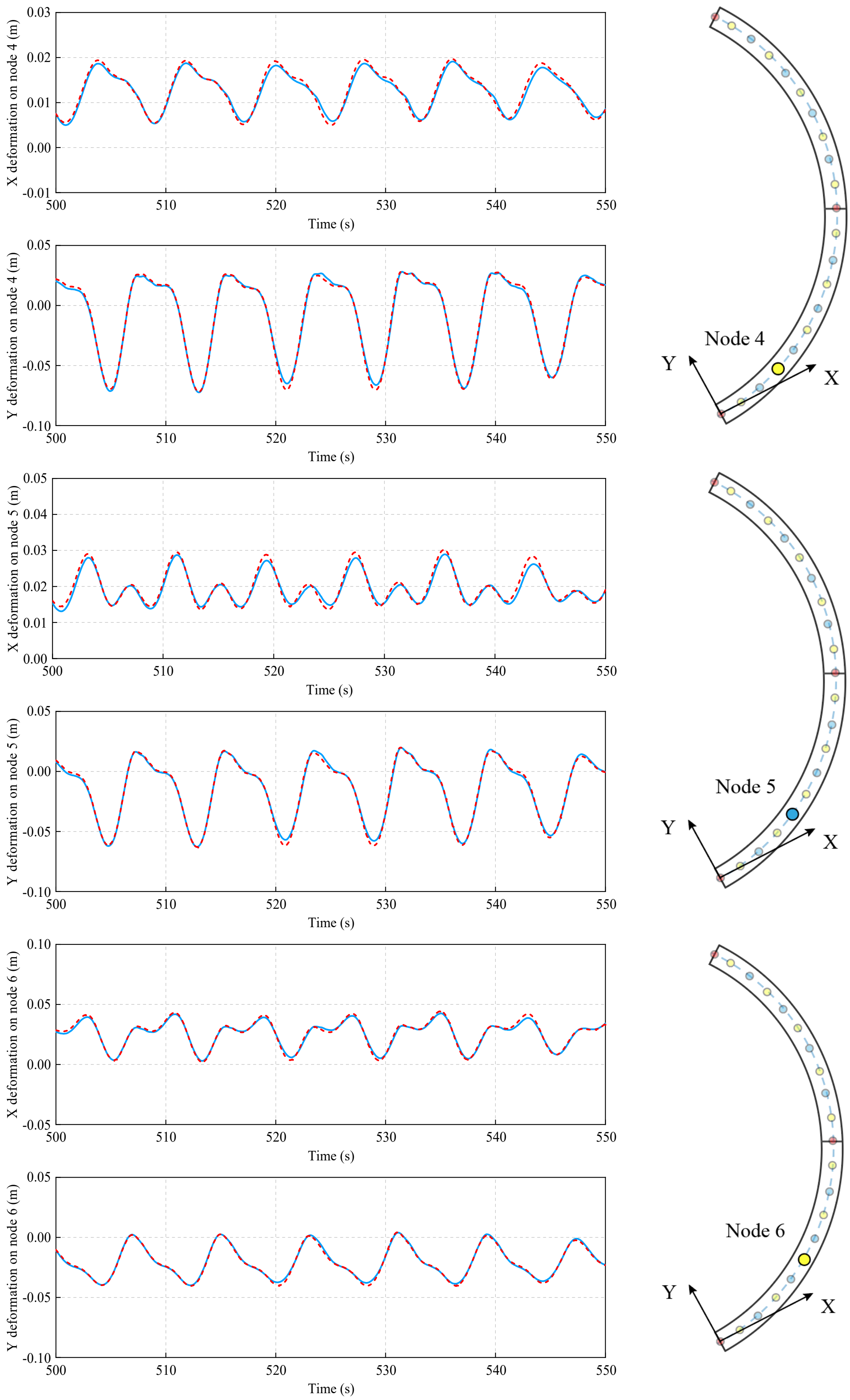
X deformation on node 4 (m)
Y deformation on node 4 (m)
X deformation on node 5 (m)
Y deformation on node 5 (m)
X deformation on node 6 (m)
Y deformation on node 6 (m)
Time (s)
Node 4
Node 5
Node 6
X
Y

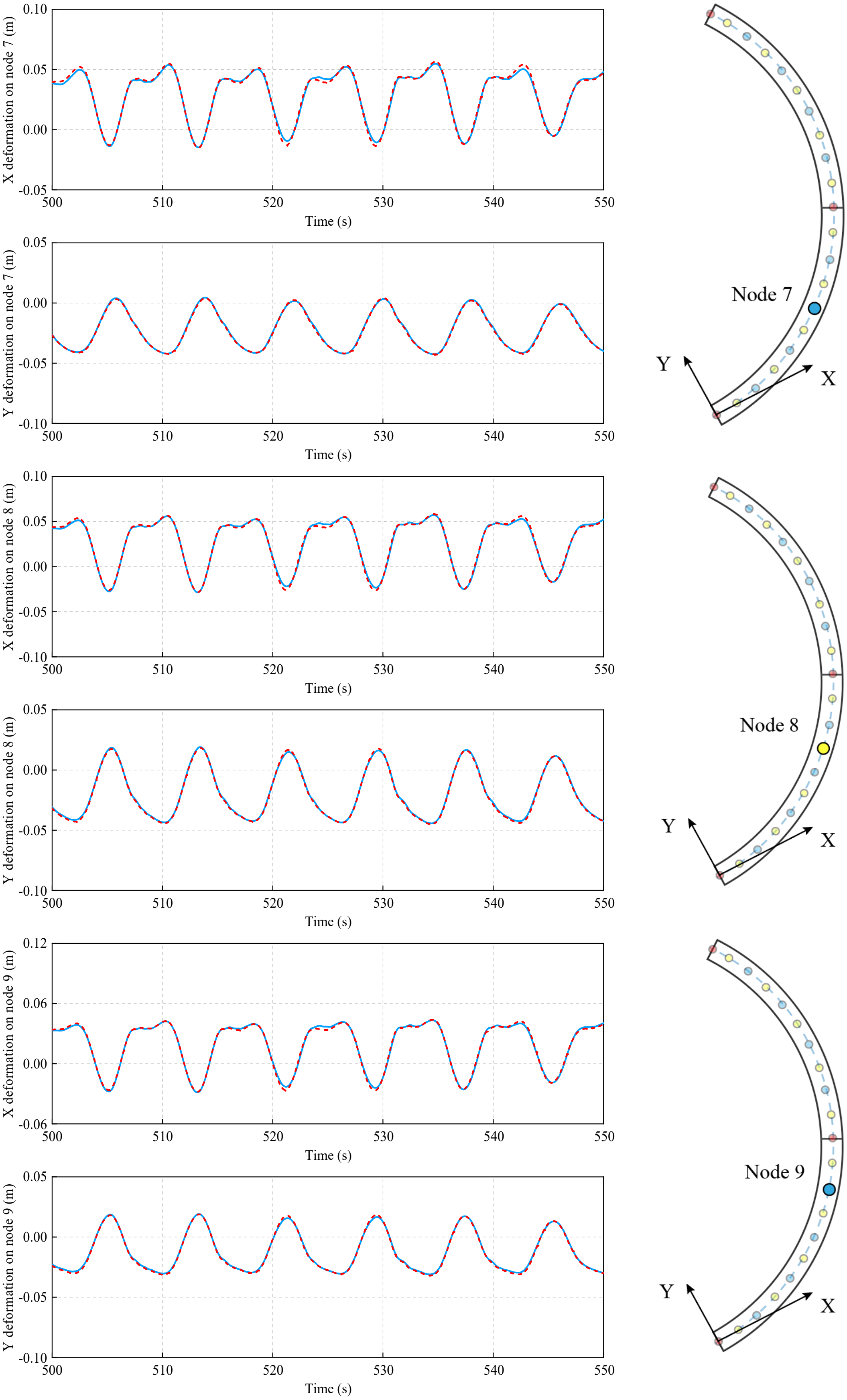
X deformation on node 7 (m)
Y deformation on node 7 (m)
X deformation on node 8 (m)
Y deformation on node 8 (m)
X deformation on node 9 (m)
Y deformation on node 9 (m)
Time (s)
0.10
0.05
0.00
-0.05
-0.10
0.12
0.06
-0.06
500
510
520
530
540
550
Node 7
Node 8
Node 9
Y
X

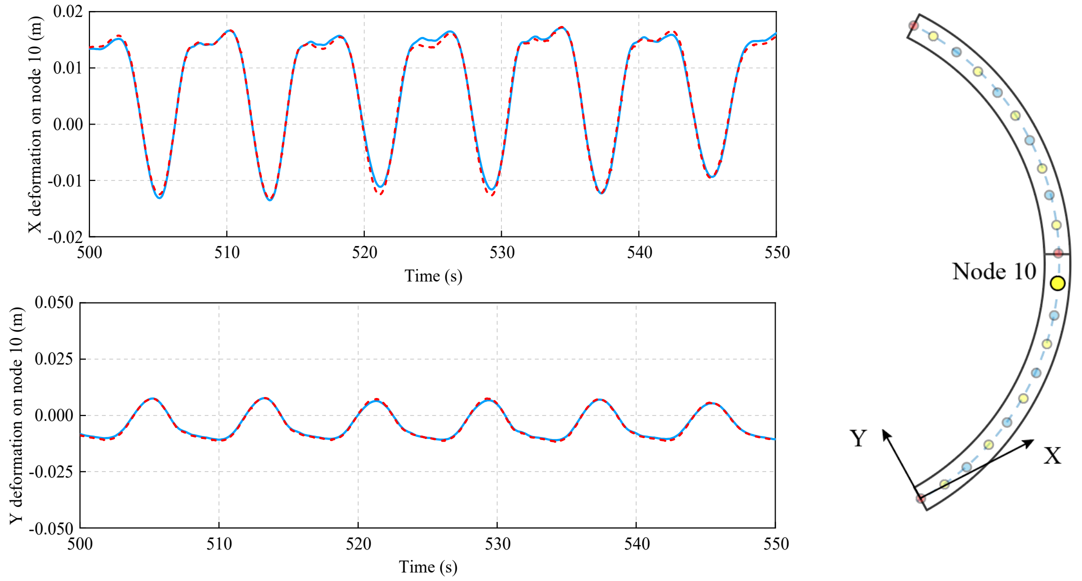

Fig. 16 Comparison of temporal histories

5.3 Spatial features

Subsection 5.2 discusses the temporal features of the helical blade deformations. This subsection focuses on spatial information. In Fig. 17, heatmaps are used to compare the spatial trajectories of the composite deformation for blade nodes throughout one rotational period of the rotor. The composite deformation on a blade node can be given by:

$$p_c = \sqrt{{p_x}^2 + {p_y}^2} \tag{29}$$

where p_x and p_y are the node deformations in x and y directions.

The horizontal axis of the figure represents the time points in one rotational period. The rotational period is approximately 8.1 s, corresponding to 81 points on the horizontal axis. The vertical axis includes all 21 blade nodes. Consequently, a total of 81×21=1701 contour points are used to illustrate the spatial features. The contour points become more yellow as the blade deformation increases.

As shown in the figure, the two heatmaps are almost identical throughout the whole region, confirming the accuracy of the SVST-ANN model in spatially presenting blade deformation behaviors. Recall from subsection 5.2 that a slight bias on node 2 of the blade deformation in the x-direction is noted. However, this phenomenon could not be observed in Fig. 17. This discrepancy occurs because the deformation in the x-direction is negligibly small compared to that in the y-direction, thus contributing little to the composition of blade deformations.

Moreover, it is noticeable that the deformation pattern of the helical blade is intricate. Three slender areas positioned at the top, middle, and bottom of the figure are dark blue, indicating zero blade deformation due to the restriction of the struts. The upper and lower halves of blade deformations show a similar pattern with a phase shift. This phase shift arises from the helical twist angle effect. The phase angle of the helical blade airfoil varies continuously from the bottom to the top, leading to a corresponding phase shift in blade deformations as the rotor rotates.

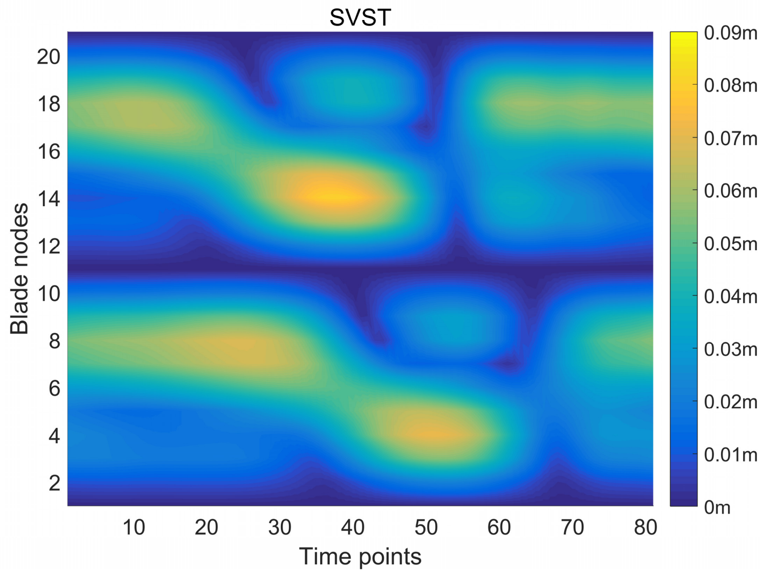

(a)

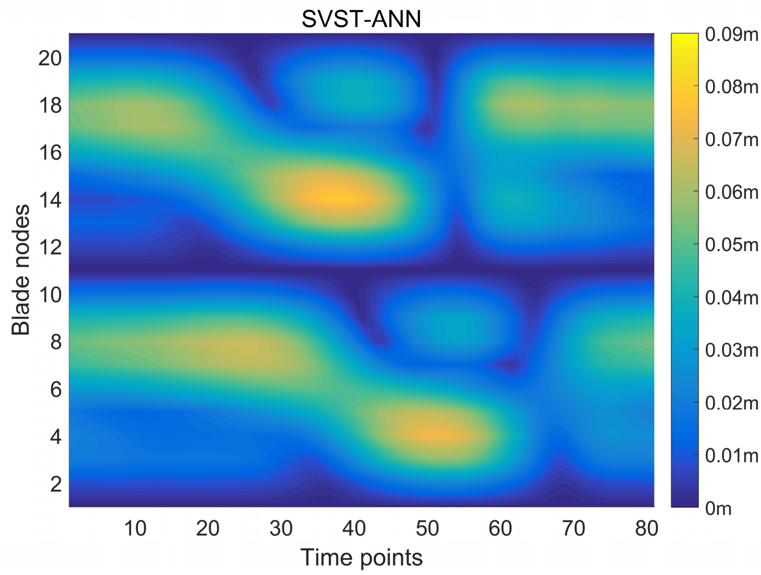

(b)

Fig. 17 Comparison of spatial trajectories (a) SVST model (b) SVST-ANN model

5.4 Statistical results

In this subsection, the statistical results are compared to quantify the accuracy of the SVST-ANN model in predicting blade deformations. Fig. 18 presents a box plot of blade composite deformations on all nodes. The deformations on nodes 1, 11 and 21 are not given because they are all zeros. The lower and upper limits of the box indicate the 25th and 75th percentiles, and the middle line within the box denotes the average value. In addition, the upper and lower boundaries of the whiskers represent the maximum and minimum values of the data. Overall, the statistical results of the two datasets show no significant differences.

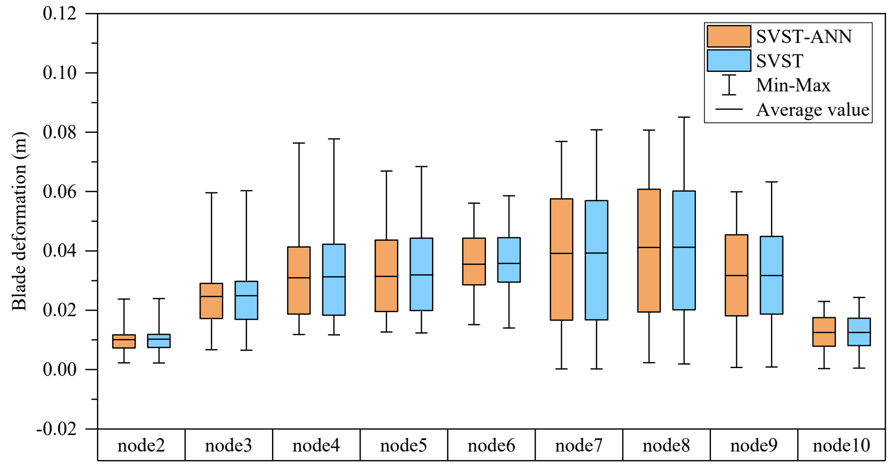

(a)

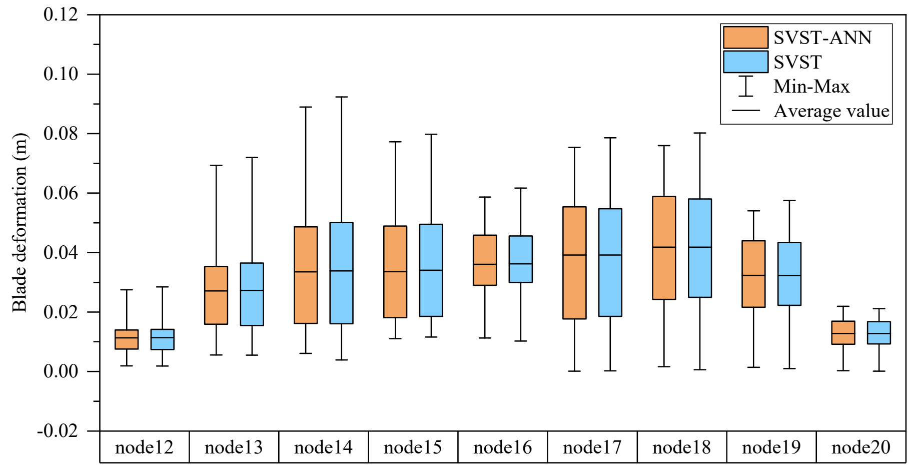

(b)

Fig. 18 Comparison of statistical results (a) from node2 to node10 (b) from node 12 to node 20

Furthermore, Table 7 details the percentage bias of the SVST-ANN model, given by the statistical results of the blade node deformations:

$$P_{MAX} = \frac{\left| MAX_{SVST} - MAX_{SVST-ANN} \right|}{MAX_{SVST}} \times 100\% \tag{30}$$

$$P_{AVE} = \frac{\left| AVE_{SVST} - AVE_{SVST-ANN} \right|}{AVE_{SVST}} \times 100\% \tag{31}$$

$$P_{STD} = \frac{\left| STD_{SVST} - STD_{SVST-ANN} \right|}{STD_{SVST}} \times 100\% \tag{32}$$

where MAX, AVE, and STD represent the maximum value, average value, and standard deviation.

Table 7 shows that the maximum percentage bias of the maximum value, average value, and standard deviation are 6.13%, 1.35%, and 0.97%, which occur at node 19, node 5, and node 2, respectively. The percentage bias of the maximum value is relatively large, demonstrating that the SVST-ANN model still exhibits a small degree of error in predicting the instantaneous blade deformations. However, the maximum percentage bias of the maximum value is less than 7%. In addition, most of the percentage biases of the average value and standard deviation are less than 1%.

Table 7 Statistical results of blade deformations

Node position	Maximum value (%)	Average value (%)	Standard deviation (%)
1	-	-	-
2	0.49	1.27	0.97
3	0.62	0.99	0.63
4	0.13	1.04	0.13
5	0.98	1.35	0.68
6	4.23	1.00	0.87
7	4.86	0.68	0.66
8	5.10	0.34	0.11
9	5.23	0.19	0.20

10	5.59	0.23	0.39
11	-	-	-
12	3.24	0.29	0.28
13	3.67	0.44	0.30
14	3.73	0.74	0.39
15	3.24	1.10	0.25
16	4.90	0.75	0.88
17	4.16	0.45	0.48
18	5.33	0.12	0.17
19	6.13	0.12	0.03
20	4.38	0.10	0.30
21	-	-	-

5.5 Computational time

The above comparisons in subsections 5.2-5.4 demonstrate the accuracy of the SVST-ANN model from different perspectives. In this subsection, the computational times of the two models are compared. The results are shown in Table 8 and Fig. 19.

For clarity, the computational time of the SVST model is divided into two parts: SVST-Configuration1 and SVST-Configuration2. In contrast, the computational time of the SVST-ANN model is divided into three parts: SVST-Configuration1, SVST-Configuration2 and ANN. As mentioned above, the SVST-Configuration1 module has no difference between the two models, so the time consumption is nearly equivalent. The major difference in the computational time lies in SVST-Configuration2. For the SVST-ANN model, when fewer blade elements are divided, the computational time is substantially reduced. Although the ANN module is added, it costs little time compared with the other two modules, as shown in Table 8 and Fig. 19. Therefore, the total time cost of the SVST-ANN model is approximately two-fifths that of the SVST model.

Table 8 Comparison of the computational time of the SVST and SVST-ANN models

Model	SVST-Configuration1	SVST-Configuration2	ANN	Total
SVST	3606.2 s	40328.6 s	-	43934.8 s
SVST-ANN	3612.7 s	13309.2 s	1.7 s	16923.6 s

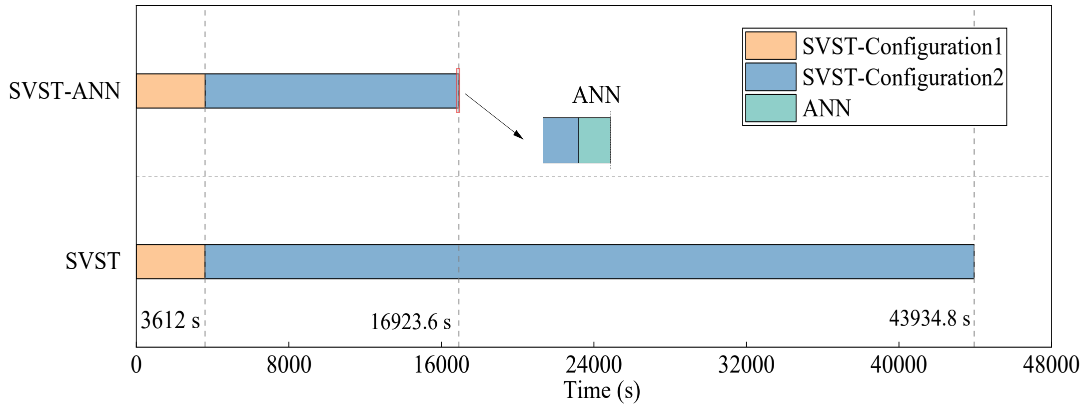

Fig. 19 Bar graph comparison of the computational time of the SVST and SVST-ANN models

5.6 Prediction ability of SVST-ANN model under different conditions

Subsections 5.2-5.5 have demonstrated that the SVST-ANN model can accurately and efficiently predict blade deformations. However, the testing case LC 2.1 is similar to the training cases. It is essential to explore whether the SVST-ANN model can effectively forecast blade deformations under significantly different environmental conditions. Therefore, time-domain simulations for the two models were conducted under LC 2.2, LC 2.3 and LC 2.4, and the statistical results of blade deformations were analyzed. Note that in this testing process, the SVST-ANN model was not retrained. This means that the model did not learn anything from load cases of LC 2.2, LC 2.3 and LC 2.4.

Table 9 summarizes the maximum percentage bias of the maximum value, average value, and standard deviation across all blade nodes. Results under LC2.1 are also listed for comparison. The table shows that the blade deformations computed by the SVST-ANN model have small errors compared to the SVST model despite changes in wind speed, rotational speed, wind turbulence intensity, and wave parameters under various cases. Consequently, it can be concluded that the SVST-ANN method still has high accuracy in predicting blade deformations for helical type FVAWTs under significantly different environmental conditions. This may be because the SVST-ANN hybrid model uses blade deformations rather than environmental parameters as input data, indicating that its predictive ability is not directly correlated with environmental conditions.

Table 9 Statistical results of blade deformations under different conditions

Load cases	Maximum value (%)	Average value (%)	Standard deviation (%)
LC 2.1	6.13	1.35	0.97
LC 2.2	4.00	2.06	1.61
LC 2.3	3.52	1.39	1.44
LC 2.4	4.38	1.41	1.81

6 Conclusions and future work

To explore the potential of large-scale FVAWT for future commercialization, it is crucial to calculate the blade deformations using an accurate and effective method. To achieve this goal, a novel hybrid SVST-ANN model was originally proposed in this study. The hybrid model is composed of SVST and ANN modules. The SVST module is used to model the wind turbine system and calculates the motions of the floater, deformations of the tower, and deformations on part of the blade elements; The ANN module is used to predict deformations on other blade elements with the input from the SVST module.

A series of comparative studies were conducted to evaluate the SVST-ANN model, utilizing a test example of a 10 MW helical-type FVAWT. According to the numerical results, the SVST-ANN model presents impressive advantages in two aspects:

(1) For machine learning techniques, many previous studies utilized environmental parameters as inputs to forecast wind turbine dynamic responses, but a direct long-term prediction is challenging due to the accumulation of errors over time. Compared to previous studies, the SVST-ANN model uses part of the blade deformations calculated by the SVST module as input data. Using this method, a strong

mapping can be established between the input and output of the ANN. This approach can circumvent the obstacle arising from the cumulative error effect, so that the long-term prediction of blade deformations can be realized.

(2) Another advantage of the SVST-ANN model is attributed to the combination of dynamic theory and machine learning techniques. The dynamic theory provides a theoretical basis for the blade responses, so that blade deformations can be precisely calculated. Machine learning techniques can greatly reduce the computational time. For example, under testing case LC 2.1, the maximum errors for the maximum value, average value, and standard deviation across all blade nodes are 6.13%, 1.35%, and 0.97%, respectively, and the computational time can be reduced by approximately 60%, showing a significant improvement in efficiency. Additionally, the SVST-ANN model maintains high accuracy under significantly different environmental conditions.

It should be noted that this study employed a large-scale helical type FVAWT for two reasons. First, the helical-type FVAWT is a promising concept for future commercial applications because it can overcome the limitations of large torque fluctuations and poor self-starting performance of the traditional H-type FVAWT. The other reason is that the modeling and calculating process of the helical blade is quite complex, so that a highly efficient simulation tool is urgently needed. Although the helical-type FVAWT was used as an example, the hybrid SVST-ANN model proposed in this study is feasible for other types of FVAWTs and FHAWTs because these floating wind turbines have similar structural compositions.

In the future, there will be advancements in the technique presented in this study. The accuracy of the SVST-ANN model will further improve, especially for some nodes near the bottom of the blade, where the blade deformations are significantly different in the x- and y-directions.

Acknowledgement

This study was supported by the National Natural Science Foundation of China (No. 51879190).

References

[1] Darwish AS, Al-Dabbagh R. Wind energy state of the art: present and future technology advancements. Renew Energy Environ Sustain 2020;5:7. https://doi.org/10.1051/rees/2020003

[2] Patryniak K, Collu M, Coraddu A. Multidisciplinary design analysis and optimisation frameworks for floating offshore wind turbines: State of the art. Ocean Engineering 2022;251:111002. https://doi.org/10.1016/j.oceaneng.2022.111002

[3] Yang C, Cheng Z, Xiao L, Tian X, Liu M, Wen B. A gradient-descent-based method for design of performance-scaled rotor for floating wind turbine model testing in wave basins. Renewable Energy 2022;187:144-55. https://doi.org/10.1016/j.renene.2022.01.068

[4] Council, G. W. E. GWEC Global Wind Energy Council Report. 2023. Global Wind Energy Council: São Paulo, Brazil

[5] Wang Y, Sun X, Dong X, Zhu B, Huang D, Zheng Z. Numerical investigation on aerodynamic performance of a novel vertical axis wind turbine with adaptive blades. Energy Conversion and Management 2016;108:275-86. https://doi.org/10.1016/j.enconman.2015.11.003

[6] Hand B, Cashman A. A review on the historical development of the lift-type vertical axis wind turbine: From onshore to offshore floating application. Sustainable Energy Technologies and Assessments 2020;38:100646. https://doi.org/10.1016/j.seta.2020.100646

[7] South P, Rangi RS. Preliminary tests of a high speed vertical axis windmill model. 1971. National Research Council of Canada.

[8] South P, Rangi RS. A wind tunnel investigation of a 14ft. diameter vertical axis windmill. 1972. National Research Council of Canada.

[9] Paraschivoiu I. Wind turbine design: with emphasis on Darrieus concept. 2002. Presses inter Polytechnique.

[10] Sheldahl R E, Klimas P C, Feltz L V. Aerodynamic performance of a 5-metre-diameter Darrieus turbine with extruded aluminum NACA-0015 blades.

1980. USA: National Technical Information Service.

[11] WORSTELL M. Aerodynamic performance of the DOE/Sandia 17-m vertical axis wind turbine in the two-bladed configuration. 1980. Wind Energy Conference.

[12] Berg DE. Structural design of the Sandia 34-meter vertical-axis wind turbine. 1985. Sandia National Laboratories.

[13] Sutherland H J. Final project report: High-energy rotor development, test and evaluation. 1996. Sandia National Laboratories.

[14] Möllerström E, Gipe P, Beurskens J, Ottermo F. A historical review of vertical axis wind turbines rated 100 kW and above. Renewable and Sustainable Energy Reviews 2019;105:1-13. https://doi.org/10.1016/j.rser.2018.12.022

[15] Buljan A. Offshore wind could grow 56-fold by 2050 and significantly contribute to green hydrogen production, DNV's new report says. 2022. https://www.offshorewind.biz/2022/10/13/offshore-wind-could-grow-56-foldby-2050-contribute-to-green-hydrogen-production/.

[16] Vestas. Vestas V236-15.0 MWTM. 2022. https://www.vestas.com/en/products/offshore/V236-15MW. accessed 2.27.22

[17] Soares-Ramos E, Oliveira-Assis L, Sarrias-Mena R, Fernández-Ramírez L. Current status and future trends of offshore wind power in Europe. Energy 2020;202:117787. https://doi.org/10.1016/j.energy.2020.117787

[18] Muhammad OS, Paul RF, Philipp B, Hans K, Amir R N, Jan W. Wind turbine nacelle testing: State-of-the-art and development trends. Renewable and Sustainable Energy Reviews 2023;188:113767. https://doi.org/10.1016/j.rser.2023.113767

[19] Apelfröjd S, Eriksson S, Bernhoff H. A Review of Research on Large Scale Modern Vertical Axis Wind Turbines at Uppsala University. Energies 2016;9:570. https://doi.org/10.3390/en9070570

[20] Mengjie L, Xin J, Yong Y, Yiming C. Bidirectional vibration control for fully-coupled floating offshore wind turbines. Ocean Engineering 2024;292:116523. https://doi.org/10.1016/j.oceaneng.2023.116523

[21] Liu J, Lin H, Zhang J. Review on the technical perspectives and commercial viability of vertical axis wind turbines. Ocean Engineering 2019;182:608-26. https://doi.org/10.1016/j.oceaneng.2019.04.086

[22] The DeepWind project. 2024. URL: https://www.deepwind.eu/

[23] SeaTwirl. SeaTwirl's S2x. 2024. https://seatwirl.com/products/seatwirl-s2/

[24] Cahay M, Luquiau E, Smadja C. Use of a Vertical Wind Turbine in an Offshore Floating Wind Farm. Offshore Technology Conference Proceedings 2011;3. https://doi.org/10.4043/21705-MS

[25] Collu M, Brennan F, Patel M. Conceptual design of a floating support structure for an offshore vertical axis wind turbine: the lessons learnt. Ships and Offshore Structures 2014;9:3-21. https://doi.org/10.1080/17445302.2012.698896

[26] Kumar PM, Sivalingam K, Lim TC, Ramakrishna S, Wei H. Review on the evolution of darrieus vertical axis wind turbine: Large wind turbines. Clean Technologies 2019;1(1):205–223. https://doi.org/10.3390/cleantechnol1010014

[27] Wen B, Tian X, Jiang Z, Li Z, Dong X, Peng Z. Monitoring blade loads for a floating wind turbine in wave basin model tests using Fiber Bragg Grating sensors: A feasibility study. Marine Structures 2020;71:102729. https://doi.org/10.1016/j.marstruc.2020.102729

[28] Xinmeng Z, Yanlin S, Xingya F, Kun X, Ruijia J, Huajun L. Nonlinear hydrodynamics of floating offshore wind turbines: A review. Renewable and Sustainable Energy Reviews 2024;191:114092. https://doi.org/10.1016/j.rser.2023.114092

[29] Borg M, Collu M. A Comparison on the Dynamics of a Floating Vertical Axis Wind Turbine on Three Different Floating Support Structures. Energy Procedia 2014;53:268-79. https://doi.org/10.1016/j.egypro.2014.07.236

[30] Owens BC, Hurtado JE, Paquette JA, Griffith DT, Barone M. Aeroelastic modeling of large off-shore vertical-axis wind turbines: Development of the offshore wind energy simulation toolkit. Proceedings of the 54th AIAA Structures, Structural Dynamics and Materials Conference 2013. https://doi.org

/10.2514/6.2013-1552

[31] Wang K, Moan T, Hansen MOL. Stochastic dynamic response analysis of a floating vertical-axis wind turbine with a semi-submersible floater. Wind Energy, 2016;19:1853-1870. https://doi.org/10.1002/we.1955

[32] Cheng Z, Madsen HA, Gao Z, Moan T. A fully coupled method for numerical modeling and dynamic analysis of floating vertical axis wind turbines. Renewable Energy 2017;107:604-19. https://doi.org/10.1016/j.renene.2017.02.028

[33] Deng W, Gao X, Liu L, Zhao H. Dynamic Modeling of H-Type Floating VAWT Considering the Rigid-Flexible Coupling Motions. ASME 2018 37th International Conference on Ocean Offshore and Arctic Engineering 2018; 78619. https://doi.org/10.1115/omae2018-78619

[34] Deng W, Yu Y, Liu L, Guo Y, Zhao H. Research on the dynamical responses of H-type floating VAWT considering the rigid-flexible coupling effect. Journal of Sound and Vibration 2019;469:115162. https://doi.org/10.1016/j.jsv.2019.115162

[35] Deng W, Liu L, Li Y, Zhang R, Li H. Slack coupled modeling method and dynamic analysis on floating vertical axis wind turbine with helical blades. Ocean Engineering 2022;246:110616. https://doi.org/10.1016/j.oceaneng.2022.110616

[36] Chollet F. Deep learning with Python. 2021. Simon and Schuster.

[37] Stetco A, Dinmohammadi F, Zhao X, Robu V, Flynn D, Barnes M, et al. Machine learning methods for wind turbine condition monitoring: A review. Renewable Energy 2019;133:620-35. https://doi.org/10.1016/j.renene.2018.10.047

[38] Wang H, Li G, Wang G, Peng J, Jiang H, Liu Y. Deep learning based ensemble approach for probabilistic wind power forecasting. Applied Energy 2017;188:56-70. https://doi.org/10.1016/j.apenergy.2016.11.111

[39] He Q, Wang J, Lu H. A hybrid system for short-term wind speed forecasting. Applied Energy 2018;226:756-71. https://doi.org/10.1016/j.apenergy.2018.

06.053

[40] de N Santos F, D'Antuono P, Robbelein K, Noppe N, Weijtjens W, Devriendt C. Long-term fatigue estimation on offshore wind turbines interface loads through loss function physics-guided learning of neural networks. Renewable Energy 2023;205:461-74. https://doi.org/10.1016/j.renene.2023.01.093

[41] Chen Y, Su J, Han Z, Zhao Y, Zhou D, Yang H, et al. A shape optimization of ϕ-shape Darrieus wind turbine under a given range of inlet wind speed. Renewable Energy 2020;159:286-99. https://doi.org/10.1016/j.renene.2020.05.038

[42] Karimian SMH, Abdolahifar A. Performance investigation of a new Darrieus Vertical Axis Wind Turbine. Energy 2020;191:116551. https://doi.org/10.1016/j.energy.2019.116551

[43] Sergiienko NY, da Silva LSP, Bachynski-Polić EE, Cazzolato BS, Arjomandi M, Ding B. Review of scaling laws applied to floating offshore wind turbines. Renewable and Sustainable Energy Reviews 2022;162:112477. https://doi.org/10.1016/j.rser.2022.112477

[44] Wanru D, Liqin L, Guo Y, Li H. Effect of helical twist angle on the aerodynamic performance and blade dynamic characteristics of floating vertical axis wind turbines. Marine Structures 2022;83:103172. https://doi.org/10.1016/j.marstruc.2022.103172

[45] YU W, MüLLER K, LEMMER F. Deliverable D4.2 Public Definition of the Two LIFES50+ 10MW Floater Concepts. 2018. Stuttgart: University of Stuttgart.

[46] Li Y, Liu L, Guo Y, Deng W. Numerical Prediction on the Dynamic Response of a Helical Floating Vertical Axis Wind Turbine Based on an Aero-Hydro-Mooring-Control Coupled Model. Energies 2022;15,3726. https://doi.org/10.3390/en15103726

[47] Tupling SJ, Pierrynowski MR. Use of cardan angles to locate rigid bodies in three-dimensional space. Medical and Biological Engineering and Computing 1987;25:527-32. https://doi.org/10.1007/BF02441745

[48] Liu Z, Hong J, Liu J. Finite element formulation for dynamics of planar flexible multi-beam system. Multibody System Dynamics 2009;22:1-26. https://doi.org/10.1007/s11044-009-9154-6

[49] Liu, J. Study on Dynamic Modeling Theory of Rigid-Flexible Coupling Systems. Ph.D. thesis. 2000. Shanghai Jiao Tong University.

[50] Bangga G, Dessoky A, Wu Z, Rogowski K, Hansen MOL. Accuracy and consistency of CFD and engineering models for simulating vertical axis wind turbine loads. Energy 2020;206:118087. https://doi.org/10.1016/j.energy.2020.118087

[51] W.J. Rankine. On the Mechanical Principles of the Action of Propellers. Transaction of the Institute of Naval Architects 1865;6:13-39.

[52] R. E. Froude. On the Part Played in Propulsion by Difference in Pressure. Transactions of the Institution of Naval Architects 1889;390-423.

[53] Leishman JG, Beddoes T. A Semi-Empirical model for dynamic stall. Journal of the American Helicopter society 1989;34:3-17.

[54] Bergami L, Gaunaa M. ATEFlap Aerodynamic Model, a dynamic stall model including the effects of trailing edge flap deflection. 2012. National Laboratory for Sustainable Energy. Denmark.

[55] Hansen M H, Gaunaa M, Madsen H A. A Beddoes-Leishman Type Dynamic Stall Model in State-space and Indicial Formulations. 2004. National Laboratory for Sustainable Energy. Denmark.

[56] Shires A. Development and Evaluation of an Aerodynamic Model for a Novel Vertical Axis Wind Turbine Concept. Energies 2013;6:2501-20. https://doi.org/10.3390/en6052501

[57] Larsen T J, Madsen H A. On the Way to Reliable Aeroelastic Load Simulation on VAWT’s. Proceedings of EWEA 2013.

[58] D.N.V. Wadam-Wave Analysis by Diffraction and Morison Theory SESAM User Manual. 2017.

[59] Ractliffe A.T. Validity of quasi-static and approximate formulae in the context of cable and flexible riser dynamics. Proceedings of the 4th Internation

al Conference on Behaviour of Offshore Structures 1985.

[60] Chen Y, Zhang D, Li X, Peng Y, Zhang X, Han Z, et al. Surrogate models for twin-VAWT performance based on Kriging and artificial neural networks. Ocean Engineering 2023;273:113947. https://doi.org/10.1016/j.oceaneng.2023.113947

[61] KRIEGER A, RAMACHANDRAN G K V, VITA L, et al. LIFES50+ D7.2 Design Basis. 2015. Bærum: DNV-GL.